HIPPARCHOS

The Hellenic Astronomical Society Newsletter
Volume 3, Issue 1
ISSN: 1790-9252

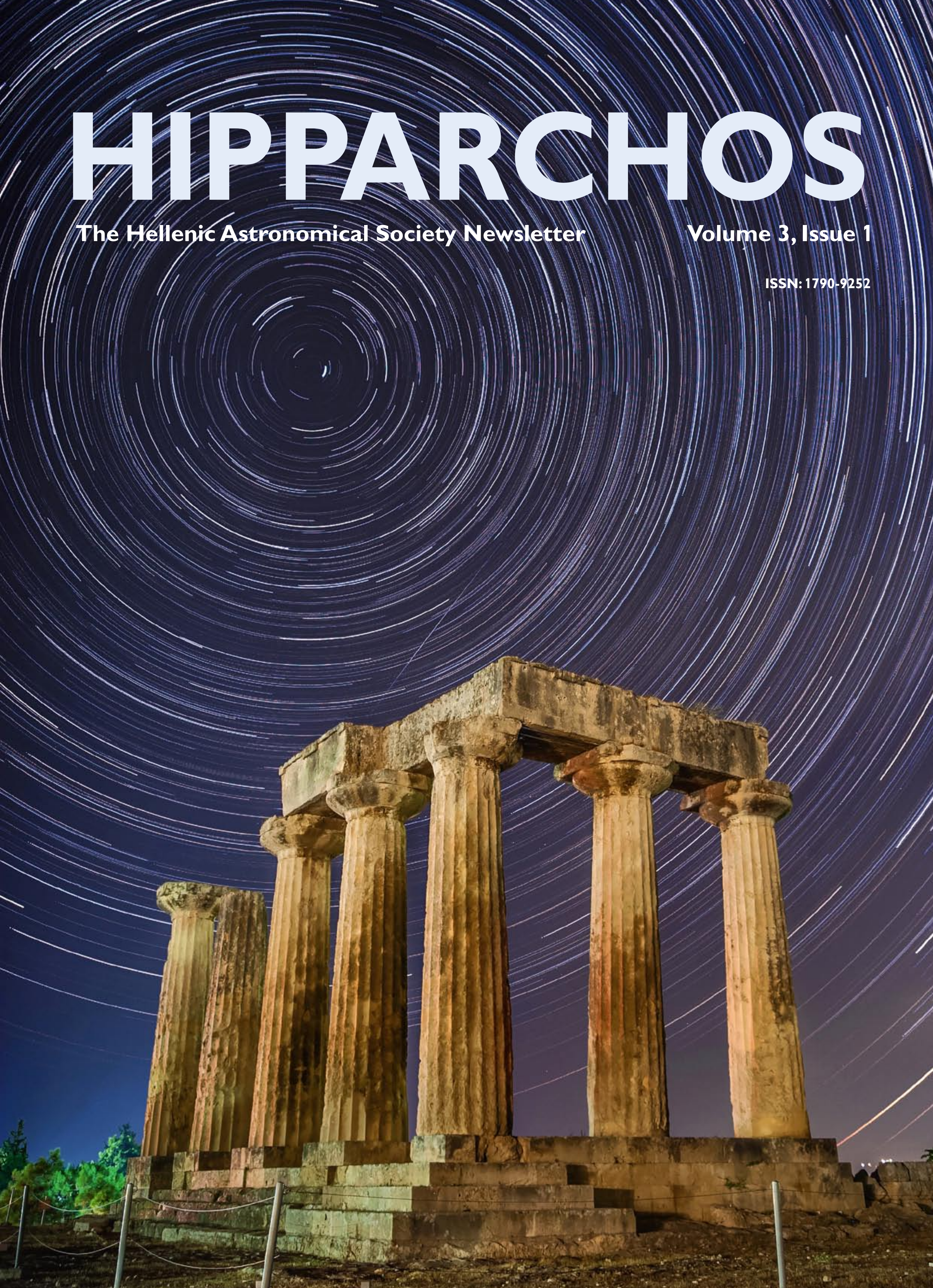

Contents

HIPPARCHOS

Volume 3, Issue 1 • June 2018

ISSN: 1790-9252

Hipparchos is the official newsletter of the Hellenic Astronomical Society. It publishes review papers, news and comments on topics of interest to astronomers, including matters concerning members of the Hellenic Astronomical Society.

Contact person
Panos Patsis
Research Center for Astronomy & Applied Mathematics (RCAAM),
Academy of Athens
Soranou Efessiou 4,
115 27 Athens, Greece
Tel: +30-210-6597-103
Fax: +30-210-6597-602
E-mail: patsis@academyofathens.gr

Printed by ZITI Publications • www.ziti.gr

Cover Image: The night sky over the Temple of Apollo at Corinth.

Credit: **Theofanis N. Matsopoulos** astrophotographer, collaborator of the European Southern Observatory.

Message from the President

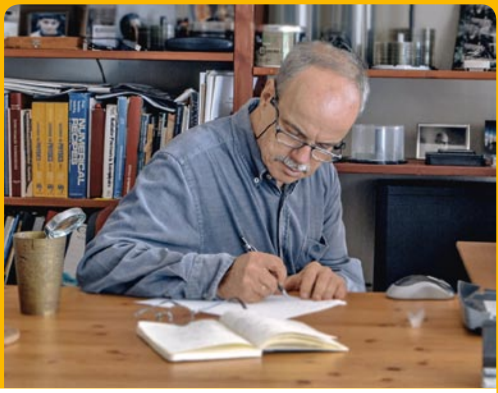

Another year, another issue of Hipparchos. Sometimes I think that we all take it for granted that the issue will appear somewhat automatically in our hands but, of course, this is not the case. So let me start in an unorthodox way by thanking all the contributors of the present issue and most of all the current Editor, Dr. Panos Patsis, for making it happen again and ensuring that the quality is up to the level we are all used to. Many thanks should also go to Mr. Theofanis Matsopoulos for his impressive cover photo.

Presenting the reviews of the current issue in a nutshell, let me start by the one of Dr. Christos Efthymiopoulos (Research Center for Astronomy, Academy of Athens). The review pertains to tides in our Solar System and makes for a fascinating read as it starts simply and gradually builds on complexity in a self-contained manner, tackling along the way some key issues of dynamical astronomy.

Dr. Nikos Prantzos (Institut d'Astrophysique de Paris) gives an in-depth review of a long-standing puzzle, namely the origin of positrons observed from the Galactic Center region. This topic has been around for decades and is closely related to some very interesting topics related to the physics of high-energy galactic sources and to cosmic-ray propagation.

Dr. Angelos Vourlidas (Johns Hopkins University) reviews two state-of-the-art solar missions, the Parker Solar Probe and the Solar Orbiter, that will revolutionize our knowledge of the inner heliosphere and solar wind. The fundamental questions that these missions will address are very interesting because they are met throughout modern astrophysics, starting right out of our cosmical doorstep and going all the way to distant quasars. By the way, the very professional review of Dr. Vourlidas reminded me that, for most countries, one of the key roles of the national Space Agencies is to keep a balance between technology and science, a policy that, I hope, will also guide the decisions of the newly founded Hellenic Space Agency.

The current issue of Hipparchos contains also a report by Dr. Nectaria Gizani (Hellenic Open University) and Dr. George Veldes (TEI of Sterea Ellada) on the Hellenic Radiotelescope. The construction of this instrument is a very positive development with many benefits for Greek Astronomy – after all, the issue of a local radio telescope has been on the Hel.A.S. agenda for about twenty years!

It will be an important omission not to mention that the past year was full of good news for Greek Astronomers. Indeed, we had one of our Members joining the US National Academy of Sciences (Dr. Vicky Kalogera), two more of our members earning European Union ERC grants (Drs Alceste Bonanos and Konstantinos Tassis) and one junior member receiving the IAU PhD Prize for 2017, Division H (Dr. Gina Panopoulou). It should be stressed that, apart from the first one, these awards were given to our Members for work performed in Greek Universities and Institutes. This expands the list that started a few years ago and by now includes the Merac Prize for best European PhD, the Einstein and von Humboldt Fellowships, the aforementioned IAU PhD Prize, just to mention some prominent ones. All these accomplishments attest to that Greek Astronomy is continuously growing, not only by the "usual suspects", namely Greek scientists of the diaspora, but also right here at home, despite the financial hardships that our Universities encountered due to consecutive budget cuts over the last decade. I strongly believe that this is not a mere statistical fluctuation, but it fully reflects the serious work undertaken. I am confident that this trend will continue in the foreseeable future.

Apostolos Mastichiadis
President of Hel.A.S.

Tides in the Solar System

by Christos Efthymiopoulos

Research Center for Astronomy and Applied Mathematics, Academy of Athens, Athens, Greece

Abstract:

Tides constitute one of the most basic dynamical phenomena responsible for sculpting the variety of spin-orbit configurations of planets and satellites encountered in our Solar System. Tides are also expected to play a major role in driving extrasolar planetary systems towards some preferential classes of spin and orbital states. In this article we present some basic notions related to tides, as applicable to celestial bodies in our Solar System, and we give a summary of related results derived after decades of theoretical research or space observations. Following some definitions, we discuss two major phenomena pertinent to tidal dynamics, namely i) tidal dissipation, and ii) spin-orbit resonances and mechanisms of capture therein. We also discuss how such phenomena can be modeled taking into account the form of tidal torques, which depend on, but also provide clues to understand, the internal properties and structure of celestial bodies in our Solar System.

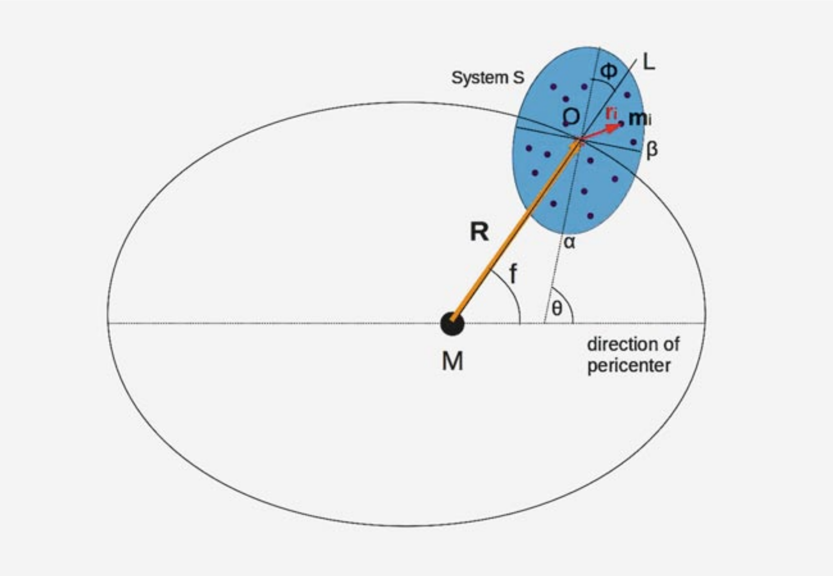

Figure 1: *Schematic representation of the basic configuration for discussing tidal (and spin-orbit) interactions between celestial bodies. A compact system S composed of N elementary masses m_i, i = 1,...N, located at positions $\mathbf{r}_i$ with respect to the center of mass O, interacts with an external mass M, which is in orbit around O. The size of S is exaggerated for visualization purposes. The blue-shaded ellipse represents the projection on the orbital plane of the moment-of-inertia ellipsoid of the system S. Assuming one of the principal axes of the inertial ellipsoid to be normal to the plane, the remaining two axes (α, β) lie in the plane. In the simplest version of the 'spin-orbit' problem, an observer placed at M approximates the orbit of S around M as a Keplerian ellipse, with M at one focus. The figure shows also notations for the various angles used to characterize the orbit and orientation of S, taken with respect to a fixed horizontal axis coinciding with the periapsis axis of the orbit.*

1. Introduction: tides among celestial bodies

Tidal interactions among celestial bodies constitute one of the most basic dynamical phenomena, believed to have played major role in sculpting the spin-orbit configurations of most planets and satellites in our Solar System. They are also expected to be important in driving extrasolar planetary systems towards some preferential classes of spin or orbital states. A detailed understanding of tides opens access to information hardly reachable by direct observations, related to the internal structure, composition and even history of formation and evolution of celestial bodies in the planetary scale. For all these reasons, understanding tidal interactions has become one of the major open goals of modern dynamical astronomy.

Basic insight into the nature of tidal interactions can be acquired using simple textbook examples of gravitating dynamical systems, in which tides constitute the driving factor of dynamical evolution. To begin with, we will consider an elementary example: N point masses m_i, $i = 1, 2, ..., N$ located within a small volume of space (see Figure 1) and interacting with each other, hereafter called the 'system' S. Let $\mathbf{r}_i$ be the particles' position vectors with respect to a point O taken to be at the center of mass of S. As internal interactions we can think of forces of any nature encountered in compact astrophysical systems, as, for example, gravity, pressure, viscoelastic forces etc. A continuous mass limit of the system S, representing a compact object like a planet, can be treated mathematically by assuming a continuous density $\rho(\mathbf{r})$ giving rise to mass elements $dm(\mathbf{r}) = \rho(r)dV$ instead of point masses, and substituting sums over particles with volume integrals in some of subsequent formulas below.

To see how tides on S can arise due to the influence of other distant bodies, consider an external body of mass M orbiting around S at (time-varying) distance R much larger than the linear size of S. As in Fig.1, let $\mathbf{R}$ denote the vector joining M with the center of mass O of S at a certain time t. The center-of-mass gravitational acceleration induced by M on S is:

$$a_{CM} = -G\left(\frac{M}{M_S}\right)\sum_{i=1}^{N}\frac{m_i(\mathbf{r}_i + \mathbf{R})}{|\mathbf{r}_i + \mathbf{R}|^3} \quad (1)$$

where $M_S = \sum_{i=1}^{N} m_i$.

Due to this acceleration, S can also be regarded as orbiting around M. Consider, now, an observer constantly attached to and accelerating with the center of mass (O) of S. Such an observer perceives the influence of M in the space surrounding O as a *differential* acceleration field, called hereafter the tidal field, given by

$$\mathbf{a}_T(\mathbf{r}) = -\frac{GM\ (\mathbf{r}+\mathbf{R})}{|\mathbf{r}+\mathbf{R}|^3} - \mathbf{a}_{CM} \qquad (2)$$

where the position vectors **r** are taken with respect to O. Multiplying tidal acceleration with mass yields a tidal force, e.g., on the particle (or mass element) *i*, given by $\mathbf{f}_{iT} = m_i \mathbf{a}_T(\mathbf{r}_i)$.

A key remark is that subtracting the center of mass acceleration allows us to deduce how the action of the external body M locally affects the configuration (and kinematics) of S. As an example, consider an almost spherical planet (e.g. the Earth) influenced by the tidal field of a satellite (e.g. the Moon, see Fig. 2 top). Referring to Figure 1, we identify the system S with the planet, and the external mass M with the planet's satellite. Assume the planet has mass M_P and mean radius R_P. The planet's center-of-mass acceleration due to the attraction by the satellite is $a_{CM} = -GM/R^2$. If we take two mass elements $m_1 = m_2 = m$ placed at antipodal points on the planet surface along the line L joining the planet with satellite, the tidal forces on these masses are:

$$f_{T,1} = -GMm\left(\frac{1}{(R-R_P)^2} - \frac{1}{R^2}\right),$$
$$f_{T,2} = -GMm\left(\frac{1}{(R+R_P)^2} - \frac{1}{R^2}\right) \qquad (3)$$

Thus, $f_{T,1} < 0$, while $f_{T2} > 0$, i.e., the tidal forces point in opposite directions (both radially outward with respect to O, see Fig. 2 top), while the two forces are equal in measure up to terms of first degree in the ratio R_P/R. This implies that the tidal field induced by the satellite tends to stretch the planet along L with nearly equal strength at antipodal points, but in opposite directions relative to O. It is worth noting that this symmetry takes place despite the fact that the body causing the tide, i.e. the satellite, is located on only one side of the planet along the line L. This is, of course, the source of the semi-diurnal (i.e. about 12 hours, or half a day) periodicity of tides on the Earth: since the tidal bulge is bisymmetric, the tidal wave travels on the Earth's surface so as to uphold a periodic-in-time surface deformation, with period nearly equal to half the period of the Earth's rotation.

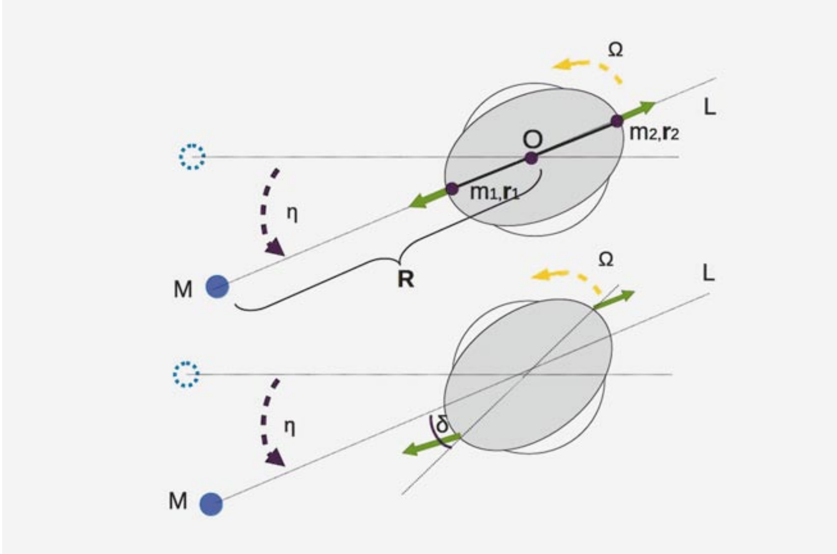

***Figure 2:** Schematic representation of the differential forces leading to the tidal deformation of a celestial body due to interaction with a satellite body. The upper part of the figure corresponds to deformation leading to the formation of an equatorial bulge with principal axis alligned with the line L. The lower part shows what happens when tidal dissipation is present. In this case, the planet's deformation can be modeled as a forced oscillation with damping. The damping causes a 'phase-lag' phenomenon, which gives rises to a permanent angular separation between the principal axis of the equatorial bulge and the line L by an angle δ. As a result, tidal forces lead to a non-zero average tidal torque. One has sgn(δ)= sgn(Ω − η). Thus, tidal dissipation causes the planet to spin down if Ω > η, or spin up if Ω < η. In the latter case, no conflict arises with the requirement of total energy dissipation (see text).*

2. Tidal torque and tidal dissipation

What are the main effects of tides on a compact celestial body such as a planet or satellite? We distinguish two major and intimately connected types of effects: i) body's deformation, and ii) perturbation of the body's spin and orbital state. Both effects are connected to *tidal torques*, to which we now turn our attention.

2.1. Tidal torque

For simplicity, assume first the compact system (or body) S to be symmetric with respect to the orbital plane [denoted as z = 0 in Cartesian co-ordinates (*x, y, z*) centered at O]. Assuming $r_i = (x_i^2+y_i^2+z_i^2)^{1/2} << R$ for all masses in S, the total torque τ exerced by M on S (with respect to the z-axis) can be computed in powers of the small quantities x_i, y_i. Up to second order we find [Goldreich & Peale (1966); see Murray & Dermott (1999)]:

$$\tau = -\frac{3}{2}\frac{GM}{R^3}(B-A)\sin 2\Phi \qquad (4)$$

where *A*, *B*, with $0<A<B$ are the moments of inertia of S around the axes *a* and *β* of Fig. respectively ($A-B$ is equal to zero if the inertial ellipsoid is axisymmetric with respect to the z-axis). This torque causes an angular momentum change in S, $\tau = dL/dt$, whose magnitude depends on the difference $B-A$. But this difference may itself be influenced by the tidal interaction, since any deformation of S caused by the tide affects the value of $B-A$. This leads to a complicated dynamical problem. Further progress can be made by examining the tidal influence on particular cases of compact systems, as discussed below.

2.2. Tidal dissipation

Tidal dissipation is the phenomenon in which the energy offered to a system by tides is partly dissipated into some form of internal energy (e.g. heat). Some major observable consequences of tidal dissipation are: i) *tidal locking*, i.e. the tendency of pairs of bodies orbiting around each other to synchronize their spin and orbital frequencies, and ii) *internal heat-*

ing that may significantly alter the internal structure of planets or satellites, and can also be related to large-scale planetary phenomena such as resurfacing and tectonics, volcanism etc. Spin-orbit synchronization is ubiquitous in our Solar System, as manifested by the locking of the spin and orbital frequencies to 1:1 (synchronous) resonance observed for planetary satellites such as the Earth's Moon, all four Galilean satellites of Jupiter (Io, Europa, Ganymedes, Callisto), the major regularly-shaped (Mimas, Enceladus, Tethys, Dione, Rhea, Titan, Iapetus) as well as several smaller satellites of Saturn, etc. A quite particular case is the planet Mercury, which presents a 3:2 rather than 1:1 resonance of the spinning and orbital frequency. Starting with the work of Giuseppe ('Bepi') Colombo [Colombo (1965)], understanding how capture to such a resonance is dynamically possible was one of the major successes of modern astrodynamics, requiring a combination of the theory of *chaotic* secular evolution of Mercury's orbital eccentricity in conjunction with the mechanism of adiabatic capture into resonance [see Correia & Laskar (2004) and references therein].

The complications for dynamics introduced by tidal dissipation can be understood by considering first two limiting cases in which such dissipation is absent:

i) *Perfectly rigid ellipsoidal body:* a perfectly rigid body corresponds to the limiting case in which the internal forces between the masses m_i in the system S are such as to constrain the shape of S to remain perfectly rigid. Such a kind of system S is hereafter called the 'rotating body'. If C denotes the moment of intertia of the rotating body with respect to the z-axis passing through O, the rotational equation of motion corresponding to the torque (4) reads

$$\frac{d^2\theta}{dt^2} = -\frac{1}{2}\eta^2\left(\frac{a}{R}\right)^3\varepsilon^2\sin 2\Phi \qquad (5)$$

where θ is the angle formed by the axis a of the inertial ellipsoid (see Fig.1), and ε is the 'asphericity factor' $\varepsilon = (3(B-A)/C)^{1/2}$. We have $\varepsilon = 0$ for a rotating body precenting cylindrical symmetry with respect to to the vertical axis passing through O, and $\varepsilon \to 1$ for a thin 'rod-like' body. In addition, a is the semimajor axis of the orbital ellipse, and $\eta = (GM/a^3)^{1/2}$ is the orbital frequency (both fixed in the limit $M_S << M$). It should be noted here that in a fully consistent treatment the orbit, with or without tidal dissipation, cannot be a perfect Keplerian ellipse, since any deformation of the rotating body induces some multipole perturbation to the interaction force between the two bodies with respect to a pure inverse square law. However, the Keplerian approximation facilitates the study and it is particularly convenient, while still quite precise in the limit $M_S << M$. At any rate, independently on the way we compute the orbital evolution, we can readily see that Eq.(5) represents a conservative law, since it can be deduced from Hamilton's equations applied to a Hamiltonian function combining both the orbital and spin degrees of freedom [see Batygin & Morbidelli (2015) for an explicit derivation of these equations when both bodies are aspherical]. In the fixed Keplerian orbit approximation, we are left only with the spin degree of freedom, and the Hamiltonian reads

$$H(\theta, p_\theta) = \\ = \frac{p_\theta^2}{2} - \frac{\eta^2\varepsilon^2}{4}\frac{a^3}{R^3(t)}\cos(2\theta - 2f(t) \qquad (6)$$

where $f(t)$ is the angle formed between the orbital vector **R** and the x-axis. As a useful convention, we take the positive x-semiaxis to point toward the pericenter of the orbital ellipse, in which case $f(t)$ coincides with the orbit's true anomaly. At any rate, the key remark is that all time-dependences in the above model are periodic (with frequency η and its multiples), thus the averaged-in-time variation of the rotational energy is equal to zero, i.e., no dissipation is produced by the time-averaged tidal torques. The same property applies in the whole hierarchy of models generated by considering various levels of the spin-orbit coupling between gravitating rigid bodies.

ii) *Body with perfectly elastic response to tidal forces*: as discussed before, in such a case, the rotating body's tidal deformation must always be alligned with the line joining M with O, thus $\tau = \psi = 0$ at all times. This implies that no angular acceleration or deceleration can be caused by the tide of M on the body. On the other hand, the elastic deformation can be described in a way analogous to Hooke's law for perfectly elastic springs or Young-type moduli describing the elastic response of rigid bodies to external forcing. In particular, the ratio of the tidal forcing over tidal deformation can be conveniently quantified by the use of *Love numbers* [Love (1927)]. Recalling the definition of the tidal acceleration given in Eq.(2), the tidal acceleration field can be obtained as gradient of a certain potential function V_T, called the *tidal potential*. By the analysis of the previous section, one deduces [see, for example, Murray & Dermott (1999)] that the lowest order term in the expansion of the tidal potential in spherical harmonics with respect to O is the quadrupole one ($l = 2, m = 0$), implying that the equipotential surfaces of the tidal potential have a prolate spheroidal form. Correspondingly, to leading degree in spherical harmonics, the tidal potential due to the external body M as measured by an observer at O is given by:

$$V_T(\mathbf{r}) = -g\zeta\left(\frac{r}{R_P}\right)^2 P_2(\cos\theta') + \dots \qquad (7)$$

In the above equation, (r, θ', φ') are spherical co-ordinates centered at O, with the angle θ' measured with respect to an axis coinciding with the line L joining M with O. Also, $g = GM_P/R_P^2$ represents the gravitational acceleration at the surface of the rotating body, of mass MP and mean spherical radius R_P. The parameter ζ has dimensions of length, and depends on the mass M and distance R of the body M as well as the radius R_P. Now, as a response to the tide, the rotating body changes its shape. Under certain assumptions (particularly justified for planets with fluid components), the deformation is also prolate spheroidal. However, this deformation implies, in turn, a small change in the multipole expansion of the gravitational potential produced by the rotating body itself with respect to the potential produced by a perfect sphere. In particular, while the equipotential surfaces of the rotating body's potential prior to the tide were spheres, following tidal deformation these surfaces become ellipsoidal. Focusing on a fixed potential value, $V_s = -GM_P/R_P$, prior to tidal deformation the associated equipotential surface is a sphere of radius R_P, while, after tidal deformation, the same potential value corresponds to an equipotential surface acquiring a prolate spheroidal form, which intersecting the previous sphere. Let h be the maximum elevation of the deformed equipotential surface V_s with respect to the sphere $r = R_P$. The maximum elevation can then be written as $h = h_2\zeta$. Finally, the whole change in the rotating's body potential outside the body due to its deformation can be described by an $l = 2$ term:

$$V_{2,body}(\mathbf{r}) = = -k_2 g\zeta \left(\frac{R_P}{r}\right)^3 P_2(\cos\theta') + \ldots \quad (8)$$

The dimensionless numbers h_2, k_2 are the Love numbers of the body subject to the tide. Their values depend on internal elasticity properties of the body. Taking, for example, the Earth, we have $h_2 \approx 0.6$, $k_2 \approx 0.3$ (see Agnew (2007) for a comprehensive review on the topic of the Earth's tides). Also, for a body of Moon's mass at Moon's distance, one finds $\zeta \sim 1$m, implying that the equilibrium tide on the Earth due to the Moon accounts for a mean tidal elevation of size ~one meter. This is a good order-of-magnitude estimate of the mean height, e.g, of the tides raised on Earth's oceans.

In general, a celestial body such as planet or satellite will present a time evolution of its moment-of-inertia ellipsoid, as well as its spin-orbit configuration, combining several features of both cases (i) and (ii) above. In particular, while case (i) provides the right framework for discussing the important phenomenon of spin-orbit resonances (see section 3 below), case (ii) provides the suitable framework for understanding how tidal dissipation enters into the game. To this end, we return to the fact that, in the absence of dissipation, regardless the rotating body's spin rate the tidal bulge has to be always aligned with the line L (Fig. 2, top), thus the angle Φ maintains always a value $\Phi = 0$. This effect can be regarded as an *in-phase* oscillatory motion of the planet, in which the tidal bulge resembles a wave inducing a non-damped oscillation of the planet's surface, with phase speed equal to twice the difference between the spin and orbital frequencies. However, as well known in the theory of damped oscillators, the presence of dissipation introduces a *phase lag*: the tidal bulge becomes misaligned with the line L by a certain angle δ (Fig. 2 bottom). The value of δ is a crucial quantity, as it accounts for a *non-zero* (averaged-in-time) tidal torque. It is precisely this non-zero torque which causes the spin down of a planet or satellite. In analogy with a corresponding quantity in the theory of damped oscillators, we define a *tidal quality factor* [Goldreich & Soter (1966)]

$$Q_T = 1/|\tan(2\delta)| \quad (9)$$

Values of Q_T for solid planets and satellites in our Solar System are estimated in the range $Q_T \sim 10$–200. This implies that the angle δ can be of the order of as much as few degrees. The occurence of a finite quality factor implies that the net (averaged-in-time) torque on the rotating body is not zero (as when $Q_T \to \infty$), but it has a value [MacDonald (1964)]

$$<\tau>_{tidal} = \frac{3}{2} k_2 \frac{GM^2 R_P^5}{a^6} \sin(2\delta) \quad (10)$$

For small angles $\sin(2\delta) \simeq \tan(2\delta) \simeq Q_T^{-1}$, implying that the net torque is inversely proportional to the tidal quality factor Q_T. On the other hand, the value of Q_T raises to $\sim 10^4$ for gaseous planets and 10^6 for stars, thus the net torque produced due to tidal dissipation becomes negligible for such objects. Finally, the sign of the net torque in equation (10) is negative if the rotating body's frequency Ω is larger than the orbital frequency η, but it is positive if $\Omega < \eta$. This latter case leads to a paradoxical situation, in which dissipation implies spin up of the rotating body, and thus an increase (rather than decrease) of the rotational kinetic energy. Physically, if $\Omega > \eta$, the tidal bulge is ahead of the orbital line L (Fig.2), thus the torque causes spin deceleration, while, if $\Omega < \eta$ the tidal bulge lags behind the orbital line L, thus the rotating body is entrained by M to rotate faster. However, regarding the overall energy balance, the paradox is resolved taking into account the effect of dissipation on the *orbit*. Namely, the total mechanical energy of the system is the sum of the rotational + orbital energy. Thus, increase of one of the two quantities can be compensated by decrease of the other. In the usual case ($\Omega > \eta$), the rotational kinetic energy decreases in time and the orbital energy increases, the overall energy variation being negative. In general, the variation of the orbital energy can be accounted for by estimates on the rate of change of the semi-major axis of the orbit (since, for a Keplerian ellipse, $E_{orbital} = -G(M_P + M)/2a$). One finds [Murray & Dermott (1999)]:

$$\frac{da}{dt} = sign(\Omega - \eta)\frac{3k_2 M}{Q_T M_P}\left(\frac{R_P}{a}\right)^5 \eta a \quad (11)$$

When $\Omega > \eta$, the semi-major axis increases in time, as for example, in the case of the Earth-Moon system ($\Omega = 2\pi/day$, $\eta = 2\pi/month$), in which precise measurements indicate a change $\dot{a} \simeq 3.7 cm/year$.

While the basic mechanical processes behind tides are intuitively clear, a detailed theory of tides requires taking into account the overall complexity of both the internal mechanisms which cause tidal dissipation as well as the orbital dynamics, which might involve more than one tide-exciting bodies. Since many aspects of the problem are related to the internal structure of the rotating body, observations are also hard to obtain or accurately justify by modelling. Basic theories and heuristic models of tides date back to George Darwin [British astronomer, son of Charles Darwin; see Darwin (1880); Darwin (1902)], while the subject was boosted by leading dynamists around the advent of the Solar System exploration era, as e.g. in the classical works of Goldreich [Goldreich (1966); see also Goldreich & Peale (1966), Goldreich & Soter (1966)], Kaula (1964), and Mignard (1979). Excellent reviews on the subject are provided in Efroimsky & Lainey (2007), and Ferraz-Mello et al. (2008). On the other hand, the tidal evolution of particular systems may be perplexed when one departs from the simple assumption of pairs of bodies tidally disturbing one the other. An astonishing example is the model of [28] regarding the tides induced by Jupiter on its closest Galilean moon, i.e. Io. It is currently believed that the outstanding volcanic activity observed in Io can be explained by a vivid tidal interaction with Jupiter: for the most, the latter is connected with the eccentricity of Io's Joviancentric orbit ($e = 0.004$) implying a 0.8% variation in the distance of Io from Jupiter between pericenter and apocenter. This variation causes a periodic tide with period equal to the orbital one (about 1.8 days). However, basic tidal theory predicts that the net tidal torque induces a *circularization* of the orbit, i.e. a decay of the orbital eccentricity, with law (for synchronous satellites)

$$\frac{de}{dt} = \frac{1-e^2}{2e}\frac{d\ln E_{orbital}}{dt} \quad (12)$$

For Io, the eccentricity damping timescale is of the order of 10^7 years, i.e., quite short related to the age of the Solar System. However, Io's eccentricity is forced to be maintained to its current value due to a different phenomenon, namely the fact that Io is part of a Laplace resonance. This is a commensurability between the orbital frequencies of Io, Europa and Ganymede, namely: $\lambda_{Io} - 3\lambda_{Eu} + 2\lambda_{Ga} \simeq \pi$. This 'three-body' resonance is conserved to greater accuracy than the pairwise 1:2 resonances between Io with Europa, and Europa with Ganymede. A detailed analysis of the secular orbital dynamics (see [3] and references therein) indicates how the Laplace resonance forces the eccentricity of Io to remain at a specific non-zero value, which is the ending point of the dissipation process instead of the value e = 0 which would result from simple orbital circularization.

3. Spin-orbit resonances and capture therein

Conventional wisdom acquired from dynamical systems' theory indicates that the ending state of a system in which dissipation is present is one of the stable states corresponding to a *resonance*, i.e., a commensurability between the system's basic frequencies. Applying these concepts to spin-orbit configurations has been a major goal in modern Celestial Mechanics. We will now refer to some basic features of resonant spin-orbit dynamics, examining first, as before, the case without dissipation. To this end, let us revisit equation (5), assuming, now, a rigid body with some non-zero asphericity ε. Almost all basic results stem from examining the factor $(a/R)^3\sin(2\Phi) = (a/R)^3\sin(2\theta-2f)$ which appears in the r.h.s of this equation. The quantities *R(t)*, *f(t)* are the radial distance from *M* and the true anomaly (angle with respect to the periapsis line) of the (assumed Keplerian) orbit. Standard expansions of Celestial Mechanics allow us to develop these quantities in series in powers of the eccentricity depending trigonometrically on the orbital phase (or 'mean anomaly' = ηt, assuming that t = 0 corresponds to pericentric passage). Implementing these series expansions we arrive at:

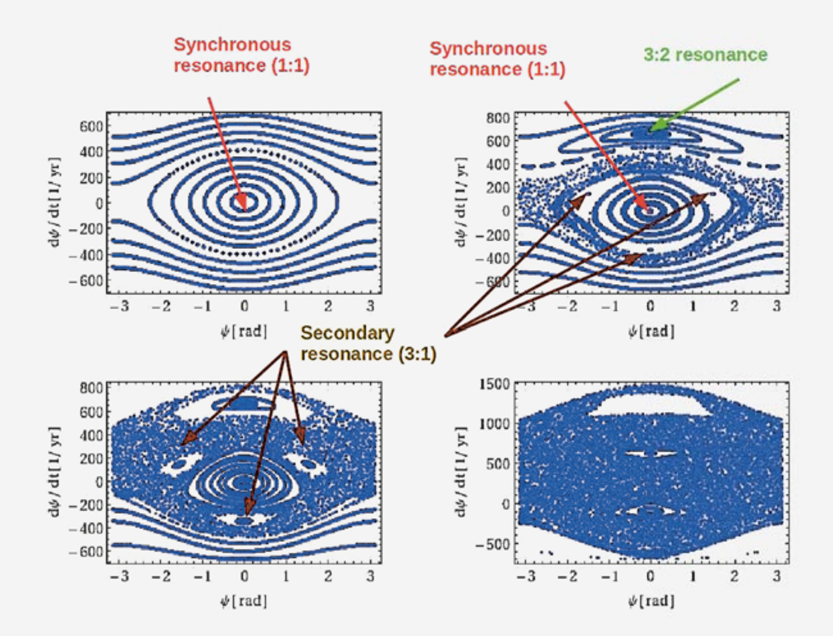

Figure 3: *The phase portrait (stroboscopic map of the angular phase velocity dψ/dt vs. the phase ψ) for the spin-orbit model of tidal interaction of a fictitious planet-satellite system, in which the planet has the mass of Saturn ($3\times10^{-4}M_\odot$ and the satellite is an object of asphericity ε = 0.4 in orbit with semi-major axis a = 5×10^5 Km and eccentricity e = 0 (top left), e = 0.02 (top right), e = 0.05 (bottom left), and e = 0.2 bottom right. Various features corresponding to primary and secondary resonances, as well as chaotic spin states are present in these figures, and all have some degree of applicability in real cases of celestial bodies in our Solar System (see text).*

$$\left(\frac{a}{R(t)}\right)^3 \sin(2\theta-2f(t)) = \quad (13)$$

$$= \sin(2\theta-2\eta t) + e\left(\frac{7}{2}\sin(2\theta-3\eta t) - \frac{1}{2}\sin(2\theta-\eta t)\right)$$

$$+e^2\left(\frac{17}{2}\sin(2\theta-4\eta t) - \frac{5}{2}\sin(2\theta-\eta t)\right)$$

We observe that the dependence of the torque on the orientation angle θ is only through the angle 2θ, which, is, again, a consequence of the fact that the leading term in the multipole expansion of the tidal torque is quadrupole. But the most important remark concerns the types of spin-orbit resonance which we can anticipate to be dynamically important from this expression: these are the following:

3.1. Synchronous (1:1) resonance

This is the most basic resonance, since it is the only resonance which produces a non-zero external driving term to spin-orbit dynamics even when the orbital eccentricity is equal to zero [see Eq. (13)]. In fact, we see that the corresponding term corresponds to a 2:2 commensurability between the orbital and spin frequencies. In anticipation of the importance of this resonance, we make a change of angular variable $\psi = 2\theta - 2f$. Then, for e = 0 the equation of motion (5) takes the form of the dynamical system:

$$p_\psi = \dot{\psi}, \quad \dot{p}_\psi = -\eta^2\varepsilon^2\sin\psi \quad (14)$$

This is just the pendulum equation. In physical terms, since $\dot{\theta} = \dot{\psi}/2 + \eta$, p_ψ measures the difference between the orbital frequency and the spin angular velocity at any time. If the rotating body is aspherical ($\varepsilon \neq 0$) for p_ψ small enough the body is trapped into a libration, i.e. the torque acts as restoring and the orientation angle θ can only librate around a value equal to the orbital phase. On the other hand, if p_ψ is large, the rotating body cannot be trapped in libration. Assuming θ = 0 at pericenter, the critical value of p_ψ is $p_{\psi,c} = 2\eta\varepsilon$. The corresponding phase portrait, with the familiar pendulum separatrix, is shown in figure 3 (top left). We observe that no other features can be distinguished for e = 0 besides the separatrix of the synchronous resonance. In particular, no chaos is present, and the spin dynamics is absolutely regular in both the librational and rotational regime. This justifies, in a very qualitative level, why the endstate of most spin-orbit systems tends to settle at the center of the synchronous resonance.

3.2. Other primary resonances: resonant interactions and chaos

The above picture changes dramatically, however, when we pass from circular to eccentric orbits, as shown in the example of the top right panel of figure 3, which corresponds to a small eccentricity e = 0.02 for the orbit of a fictitious body with parameters in a range relevant to Saturn's satellites, but large asphericity (ε = 0.4). This numerical example summarizes all interesting phenomena generated due to the fact that, for $e \neq 0$, instead of the pendulum equations (14) we obtain modulated pendulum equations, i.e.:

$$\dot{p}_\psi = -\eta^2\varepsilon^2\left[\sin\psi + e\left(\frac{7}{2}\sin(\psi-\eta t) - \frac{1}{2}\sin(\psi+\eta t)\right) + e^2\left(\frac{17}{2}\sin(\psi-2\eta t) - \frac{5}{2}\sin\psi\right)\right] \tag{15}$$

The most important modulating term is $(7e/2)\sin(\psi - \eta t) = (7e/2)\sin(2\theta - 3\eta t)$, which corresponds to the primary 3:2 spin-orbit resonance, i.e. $3\eta = 2\Omega$. This is, precisely, the resonant status of planet Mercury's spin-orbit configuration around the Sun (orbital period ≃ 58.6 days, rotation period ≃ 88 days). The asphericity of Mercury is ε ≃ 0.018 while the orbital eccentricity is e ≃ 0.2. It is, precisely, for this relatively large value (largest in all planets in the Solar System) that Mercury had a considerable probability of getting captured in the 3:2 resonance, see discussion above).

Returning to Figure 3, we see that for a largely aspherical body (such as an irregularly-shaped satellite), an orbit with eccentricity as small as 0.02 introduces an important spin-orbit 3:2 resonant modulation. In the phase portrait, the librational domain occupied by the 3:2 resonance is of comparable size as the one of the synchronous resonance. But the most spectacular feature of the phase portrait is *chaos*, produced in the overlap domain between these resonances. The chaotic zone produced between these resonances is localized around the separatrices of the resonances. However, for still larger eccentricities (0.05 and 0.2, lower panels in Figure 3) chaos dominates nearly the whole phase space. This implies that the spin state of the satellite in this regime becomes essentially unpredictable, even in short timescales. These phenomena are even more pronounced when more modulating parameters are included, e.g. orbits with high inclination, more harmonics of the planetary potential etc. A characteristic example of chaotic rotational behavior is Hyperion, an irregularly-shaped satellite of Saturn. In the case of Hyperion observations indicate that the chaotic rotation is so enhanced that the orientation of the satellite becomes practically unpredictable over timescales of the order of only about one month [see analysis and references in Tarnopolsky (2015)]. In fact, the case of Hyperion is of historical importance, since it represents the first celestial body where the dynamical state of chaos, predicted theoretically in the 80s [Wisdom et al. (1984)], was unambiguously observed.

3.3. Secondary resonances

Finally, secondary resonances around the primary resonances may play an important role. Figure 3 shows the example of the 3:1 secondary resonance bifurcating from the synchronous primary resonance. The existence of secondary resonances provides new possibilities for the endstate of tidal dissipation, or even for a long-lasting quasi-trapping to a secondary resonant state interferring the route of a planet's or satellite's approach towards it's final spin state. Such quasi-trapping may have dramatic consequences as regards the geological *history* of the planet or satellite. A prominent example is Enceladus, the second innermost regular-shaped satellite of Saturn. Based on images sent by Voyager, it was originally argued by Wisdom (2004) that Enceladus could be is a secondary 3:1 quasi-trapped state, a fact which would allow to produce a tidal heating rate of Enceladus as high as 30 times the Mimas heating rate, thus passing the "Mimas test" [Squyres et al. (1983)]. Furthermore, quasi-trapping in a secondary resonance around the synchronous primary resonance could explain the ubiquitous observational evidence for *re-surfacing* i.e., tectonic activity applying to the ice layers on the surface of this satellite. However, more recent observations by Cassini reduced Enceladus' estimated asphericity closer to $\varepsilon \approx 1/4$, rendering possible only a trapping to the 4:1 secondary resonance, which is anyway much less important than the 3:1 resonance [Porco et al. (2006)]. Alternative mechanisms, involving some locking to a forced eccentricity state (possibly in conjunction with some mean-motion resonance to another satellite of Saturn) were reviewed in [Meyer & Wisdom (2007)] and found equally unadequate. Thus, while the current produced tidal heating rate of Enceladus remains ununderstood, past episodes of peaks of the tidal heating and resulting resurfacing remain amply possible. Note that tidally-induced resurfacing is observed also in Europa (the second of the Galilean Moons), while it is evident that tidal activity is responsible, in general, for the possible maintainance of liquid oceans of water beneath the surface of both these satellites.

Finally, secondary spin-orbit resonances should be ubiquitous among solar system objects of smaller size, as, for example, double asteroids. The bifurcation of a 1:n secondary resonance takes place when the asphericity becomes of order $\varepsilon \sim 1{:}n$. Since the asphericity parameter in this case is essentially unconstrained (values as high as $\varepsilon \sim 1$) are possible, one can encounter practically the whole spectrum of secondary resonances up to 1:1, all around the synchronous primary resonance. This topic is new, and only scarce observational data are available [see, for example, Pravec et al. (2016)]. On the other hand, current theoretical developments based on high-order perturbation theory allow us to predict with accuracy the time evolution of spin states in such extreme cases of resonant spin-orbit configurations [see Gkolias et al. (2016)], while an extension of similar techniques in the spin-orbit problem with tidal dissipation [Gkolias et al. (2017)] allows us to transform the problem into one in which the techniques of adiabatic capture into resonance [Henrard (1982)] can be implemented.

Acknowledgements

Stimulating discussions with my collaborators on the problem of secondary spin-orbit resonances A. Celletti, I. Gkolias, and G. Pucacco, are gratefully acknowledged.

References

[1] Agnew, D.C.: 2007, "Earth Tides. Treatise on Geophysics and Geodesy", in Herring TA, (Ed.), pp. 163-195., Elsevier, New York.

[2] Batygin, K., and Morbidelli, A.: (2015), Astrophys. J. 810, 110.

[3] Celletti, A., Paeta, F., and Pucacco, G.: (2018), Cel. Mech. Dyn. Astron., 130, 15.

[4] Colombo, G.: 1965, Nature 208, 575.

[5] Correia, A., and Laskar, J.: 2004, Nature 429, 848.

[6] Darwin, G.H.: 1880, Philos. Trans., 171, 713

[7] Darwin, G.H.: 1902, "Tides", Lemma of the Encyclopedia Britannica

[8] Efroimsky, M., and Lainey, V.: 2007, J. Geophys. Res. 112, E12003.

[9] Ferraz-Mello, S., Rodriguez, A., and Hussmann, H.: 2008, Cel. Mech. Dyn. Astron., 101, 171.

[10] Goldreich, P.: 1966, Astron. J. 71, 1.

[11] Goldreich, P., and Peale, S.: 1966, Astron. J. 71, 425.

[12] Goldreich, P., and Soter, S.: 1966, Icarus 5, 375.

[13] Gkolias, I., Celletti, A., Efthymiopoulos, C., and Pucacco, G.: 2016, Mon. Not. Royal. Astr. Soc, 459, 1327

[14] Gkolias, I., Efthymiopoulos, C., Pucacco, G. Celletti, A.: 2017, Comm. Nonlin. Sci. Num. Sim., 51, 23.

[15] Henrard J.: 1982, Cel. Mech., 27, 3.

[16] Kaula, W.M.: 1964, Rev. Geophys., 3, 661.

[17] Love, A.E.H.: 1927, "A Treatise on the Mathematical Theory of Elasticity", Campridge University Press.

[18] MacDonald, GJE.: 1964, Rev. Geophys. Spa. Phys. 2, 467.

[19] Meyer, J., and Wisdom, J.: 2007, Icarus, 188, 535.

[20] Mignard, F.: 1979, Moon and Planets, 20, 301.

[21] Murray, C.D., and Dermott, S.F.: 1999, "Solar System Dynamics", Cambridge University Press.

[22] Porco, C.C. et al: 2006, Science, 311, 1393.

[23] Pravec et al.: 2016, Icarus, 267, 267.

[24] Squyres, S.W., Reynolds, R.T., Cassen, P.M., and Peale, S.J.: 1983, Icarus 53, 319.

[25] Tarnopolsky, M.: 2015, Astrophys. Sp. Sci., 357, 160.

[26] Wisdom, J., Peale, S.J., and Mignard, F.: (1984), Icarus, 58, 137.

[27] Wisdom, J.: (2004), Astron. J., 128, 484.

[28] Yoder, C.F., and Peale, S.J.: 1981, Icarus 47, 1.

Visit our website

http://www.helas.gr

The above web server contains information, both in greek and english, about the Hellenic Astronomical Society (Hel.A.S.), the major organization of professional astronomers in Greece. The Society was established in 1993, it has more than 250 members, and it follows the usual structure of most modern scientific societies. The web pages provide information and pointers to astronomy related material, useful to both professional and amateur astronomers in Greece. It contains a directory of all members of the Society, as well as an archive of all material published by the Society, including electronic newsletters, past issues of "Hipparchos", and proceedings of Conferences of Hel.A.S. The server is currently hosted by the University of Thessaloniki.

The chase for the Galactic positrons

by Nikos Prantzos
Institut d'astrophysique de Paris

The existence of a particle with equal mass but opposite charge to that of the electron was predicted by Dirac (1931), who named it the "antielectron." Unaware of Dirac's prediction, Anderson (1932) found the first experimental hints for such a particle in cloud-chamber photographs of cosmic rays (CR), and he called it the positron. His finding was confirmed the following year by Blackett and Occhialini (1933), who identified it with Dirac's antielectron. One year later, Klemperer and Chadwick (1934) detected the characteristic γ-ray line at 511 keV resulting from electron-positron ($e^- - e^+$) annihilation, a convincing proof that positrons are indeed electron's antiparticles. That same year, the Croatian physicist Mohorovicic (1934) predicted the existence of a bound system composed of an electron and a positron (analogous to the hydrogen atom, but with the proton replaced by a positron), which he called "electrum." This state was experimentally found by Deutsch (1951) at MIT and became known as *positronium*.

For about 30 years after their discovery, all detected positrons were of terrestrial origin. Those detected by Anderson (1932) and Blackett and Occhialini (1933) were created by cosmic-ray interactions with molecules in Earth's atmosphere. Joliot and Curie (1934) identified another positron producing process, e^+ radioactivity of artificially created unstable nuclei. The first positrons of extra-terrestrial origin were reported by de Shong et al. (1964), who loaded a spark chamber on a stratospheric balloon to detect positrons within the cosmic rays. Ginzburg (1956) had already suggested that high-energy p-p interactions in cosmic rays would produce pions π+, which would decay to positrons (via muon decays). The production rate of those pions was evaluated by Pollack and Fazio (1963) who predicted a γ-ray flux from the Galaxy at 511 keV of ~10^{-3} cm^{-2} s^{-1}.

The properties of $e^- - e^+$ annihilation were explored in the 1940s. Direct $e^- - e^+$ annihilation produces a single γ-ray line at 511 keV, while the annihilation of positronium produces a composite spectrum with a lower-energy continuum and a 511 keV line (Ore and Powell, 1949 and Fig. 1 and 2). Stecker (1969) was the first to point out that in the conditions of the interstellar medium, most positrons would annihilate after positronium formation.

The 511 keV emission of e^+ annihilation was first detected from the general direction of the Galactic center (GC) in the early 1970s, by balloon-borne instruments of low-energy resolution (Johnson et al., 1972). It was unambiguously identified a few years later with high-resolution Ge detectors (Leventhal et al., 1978). It is the first and most intense γ-ray line originating from outside the Solar System that was ever detected. Its flux on Earth (~10^{-3} cm^{-2} s^{-1}), combined with the distance to the Galactic center (~8 kpc or ~25000 light-years), implies the annihilation of 2-4 10^{43} e^+ s^{-1}, releasing a power of ~10^{37} erg s^{-1} or ~10^4 solar luminosities (L⊙) in gamma-rays. Assuming a steady state, i.e., equality between production and annihilation rates of positrons, one should then look for a source (or sources) able to provide ~2-4 10^{43} e^+ s^{-1}. If the activity of that site were maintained to the same level during the ~10 Gy of the Galaxy's lifetime, a total amount of positrons equivalent to ~3-6 solar masses (M⊙) would have been annihilated.

Imaging the Galaxy in annihilation gamma-rays was considered to be the exclusive way to identify the cosmic e^+ sources (assuming that the spatial morphology of the γ-ray emission reflects the spatial distribution of the sources, i.e., that positrons annihilate close to

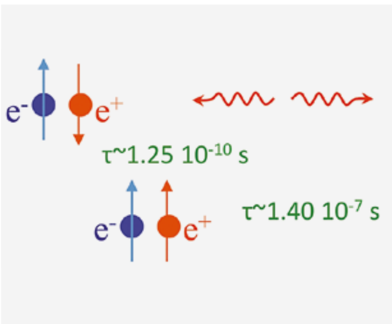

Figure 1: Para-positronium (top) and ortho-positronium (bottom). The annihilation of the electron and the positron within the given timescales gives 2 gamma-ray photons of 511 keV in the first case and a continuum of 3 photons up to 511 keV in the second case.

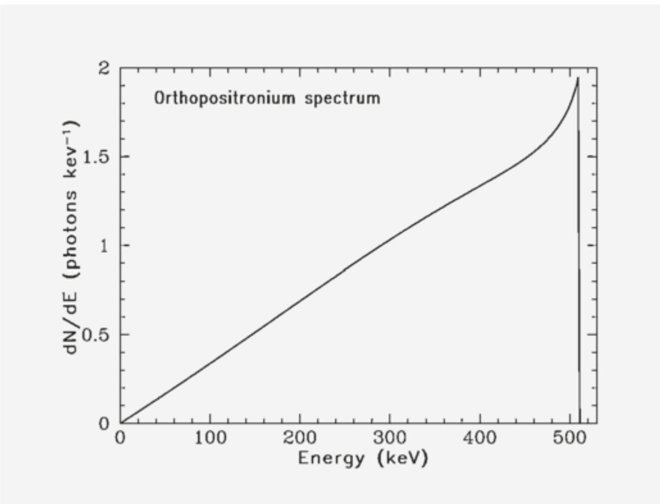

Figure 2: Spectrum of ortho-positronium annihilation with the three-photon continuum (from Ore and Powell, 1949).

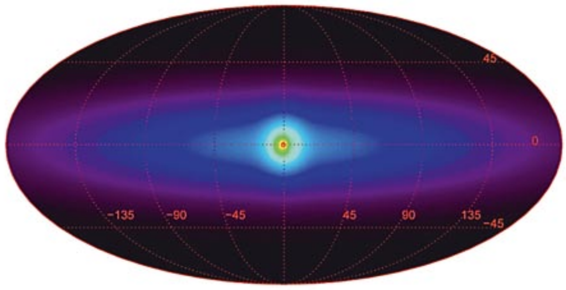

Figure 3: *The 511 keV emission of the Galaxy, after 12 years of INTEGRAL data. The bulge contributes for about 40% of the total and there are hints for a thick disk.*

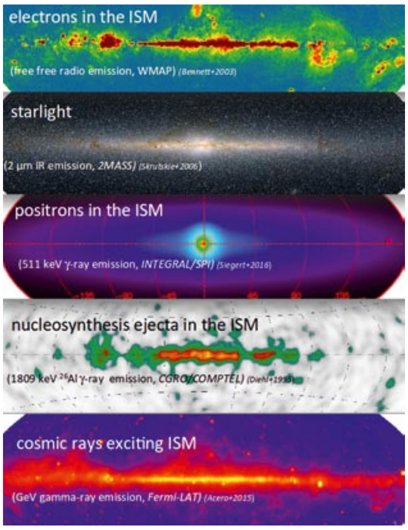

Figure 4: *The Milky Way in various wavelengths, reflecting different emission processes and sources. The disk always dominates and only in the near-infrared the old stellar population of the bulge makes a substantial contribution (~1/3 of the total).*

their production sites). Because of the difficulties of imaging in the MeV region, progress was extremely slow in that field: only in the 1990s were the first constraints on the spatial distribution of the 511 keV emission in the inner Galaxy obtained by the OSSE instrument aboard the Compton Gamma Ray Observatory (CGRO, Purcell et al., 1997). The most reliable imaging of the 511 keV emission was obtained by the SPI instrument aboard ESA's INTEGRAL Gamma Ray Observatory, after about 12 years of observations (Siegert et al. 2016). The emission is strongly concentrated in the inner Galaxy and a rather thick disk of similar or slightly higher total emissivity is found (Fig. 3), unlike the situation at any other wavelength (Fig. 4).

Several candidate sources of positrons have been proposed over the years: radioactivity from e^+ decay of unstable nuclei produced in stellar explosions, high-energy interactions occurring in cosmic rays or near compact objects (such as pulsars and x-ray binaries), or the supermassive black hole in the Galactic center, and even annihilation of dark matter particles. For a long time, radioactivity from Co-56 produced in thermonuclear supernovae (SNIa) appeared as the most promising candidate, provided that just a few per cent of the released positrons could escape the supernova remnant and annihilate in the interstellar medium. However, none of the candidate sources has a spatial pattern resembling that of the detected γ-ray emission. In particular, the release of the first year of SPI data, revealing the bulge but not yet the disk, prompted a series of "exotic" explanations involving dark matter (DM) particles, superconducting cosmic strings, etc. The confirmation of disk emission a few years later caused a loss of interest in such explanations, but they have not been completely eliminated so far.

The detailed quantitative characterisation of the different components of 511 keV emission requires parametrising these in the form of (necessarily idealised) spatial emission models fitted to the data. Such decomposition is not unique, because both the spheroid and the disk may have faint extensions contributing substantially to their total γ-ray emissivities. In the early years of INTEGRAL/SPI analyses, thin to moderately extended disk models had been tested. With more exposure, the disk emission was revealed, and it became clear why it had been difficult to detect it: in a parameter study from 13 years of observations, Siegert et al (2016) showed that the disk component appears to have a low surface brightness, although as a whole being as intense as the emission from the inner Galaxy. The bulge-to-disk flux ratio derived from these deeper observations now falls below the values B/D~1 that stimulated the above discussions of exotic origins, and is determined as B/D=0.58±0.13 (Siegert et al. 2016). The disk component of annihilation gamma rays seems quite extended, up to kpc in latitude. This suggests that positrons may fill a much larger volume than previously thought, and may annihilate as they leave the gaseous disk of the Galaxy towards the halo.

The spectral analysis of the 511 keV emission had already established in the late 1970s that most of the positrons annihilate after positronium formation (Bussard et al., 1979). This result constitutes an important diagnostic tool for the physical properties of the annihilation medium, as analyzed by Guessoum et al. (1991, see also Fig. 5). Only recently, in the 2000s, was it realized that the spectral analysis may also provide important hints on the e^+ source(s). In particular, positrons appear to annihilate at low energies, while in most candidate sources they are produced at relativistic energies. The observed flux at MeV energies from the inner Galaxy constrains the initial energy of the positrons to less than a few MeV, otherwise the emission from in-flight annihilation would exceed the observed flux (Fig. 6). Moreover, the spectral analysis provides important information on the physical properties of the e^+ annihilation sites (Siegert et al. 2016). The large positronium fraction f~95% implies that positrons annihilate mostly at low energies, since direct annihilation cross sections are important only at high energies. The overall spectral shape suggests that annihilation occurs mostly in warm (T ~8000 K) media, at about equal amounts in neutral and ionized phases but it cannot be excluded that less than 23% of annihilation occurs in the cold neutral medium (T~80 K). Annihilation in the neutral media may account for the presence of a broad 511 keV line component (FWHM~5 keV) and the annihilation in the warm ionized medium for the narrow one (FWHM~1 keV).

Among the various astrophysical

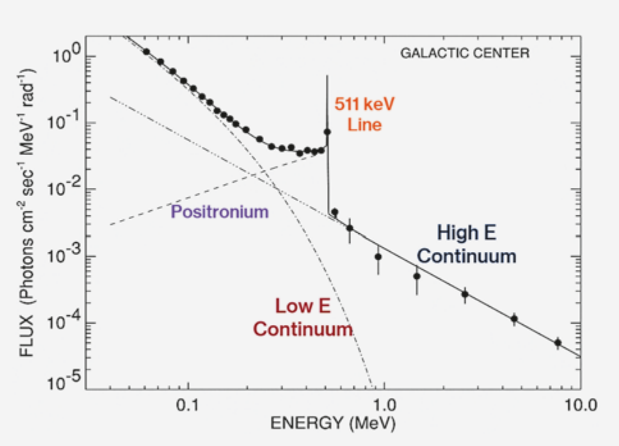

***Figure 5:** Spectrum of the Galactic Center region in low-energy gamma-rays, taken by the OSSE instrument aboard the Compton Gamma-Ray Observatory (Kinzer et al. 2001). It is fitted by a 511 keV line of electron-positron annihilation and three continuum components. The positronium component accounts for 93% of the total annihilation emission.*

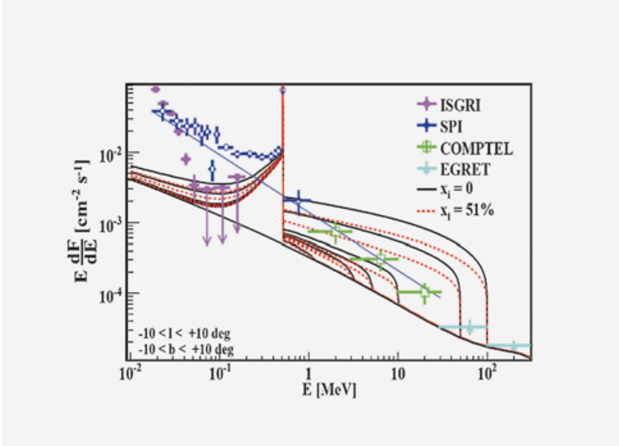

***Figure 6:** Spectrum of the inner Galaxy as measured by various instruments (data points), compared to various theoretical estimates (curves) made under the assumption that positrons are injected at high energy: the four pairs of curves result from positrons injected at 100, 30, 10 and 3 MeV (from top to bottom) and correspond to positrons propagating in neutral (solid) or 50% ionized (dotted) media (from Sizun et al., 2006). This constrains the injected positron energy (or, equivalently, the mass of the putative decaying/annihilating dark matter particles, see text) to a few MeV.*

sources of positrons proposed so far, the only one known with certainty to release e^+ in the ISM is e^+ radioactivity of Al-26 (an unstable nucleus with ~1My lifetime), because the characteristic gamma-ray line of its decay at 1.8 MeV has been observed in the Galactic disk since the 1980s; the observed intensity of its characteristic 1.8 MeV emission in the Galaxy corresponds to ~3–4 10^{42} e^+ s^{-1}. A similar amount is expected from the decay of Ti-44 – another radioactive nucleus with lifetime of ~67 yr – on the grounds of nucleosynthesis arguments (it is the unstable parent of the stable Ca-44 nucleus, the cosmic abundance of which is well known). Both radionuclides are produced mostly in massive stars and their positrons should be released along the Galactic plane, as traced by the 1.8 MeV emission (Fig. 5), they could thus account for a substantial fraction the observed disk 511 keV emission.

Radioactivity of Co-56 (with lifetime of about 2 months) from SNIa was traditionally considered to be the major e^+ producer in the Galaxy. Both the typical Co-56 yield of a SNIa and the Galactic SNIa rate are rather well constrained, resulting in ~5 10^{44} e^+ s^{-1} produced inside SNIa. If only a small fraction (~4%) of them escape the supernova remnant to annihilate in the ISM, the observed total e^+ annihilation rate can be readily explained. However, observations of two SNIa, interpreted in the framework of 1D (stratified) models, suggest that the positron escape fraction is negligible at late times. On the other hand, both observations of early spectra and 3D models of SNIa suggest that a sizeable fraction of Ni-56 (the unstable parent of Co-56) is found at high velocity (close to the surface), perhaps making the subsequent escape of positrons from Co-56 easier. Thus, SNIa remain a serious candidate, with a potential Galactic yield of 2 10^{43} e^+ s^{-1}.

Each of the candidate positron sources should be critically discussed in the light of all the observational constraints. Here we use three main criteria:

i) the total e^+ annihilation rate (~5 10^{43} s^{-1}),
ii) the typical energy of the injected positrons, or the equivalent mass of annihilating DM particles (<3 – 7 MeV) and (perhaps, most significantly)
iii) the morphology of the 511 keV emission (parameterized by a bulge/disk ratio B/D~1, higher than in all other wavelengths.

Positron production rate: Assuming a steady state regime, the e^+ annihilation rate has to be equal to the average e^+ production rate during the lifetime of positrons in the ISM. The only source definitely known to provide substantial amounts of e^+ at a well constrained rate is the radioactive decay of Al-26: 4 10^{42} e^+ s^{-1}. The decay of 44 Ti probably provides another 0.3 10^{43} e^+ s^{-1}. GCRs probably provide 0.1 10^{43} e^+ s^{-1} Nova models (as constrained against several observables such as ejecta abundances, velocities etc.) may provide a e^+ yield from the decay of radioactive Na-22 of ~10^{41} e^+ s^{-1}. The positron production of all other candidate sources is entirely speculative at present. The values reported in Table I for those sources should be considered as optimistic rather than typical ones. Indeed, no useful observational constraints exist up to now on the e^+ yields of hypernovae/GRBs, pulsars, ms pulsars, magnetars, microquasars, the supermassive black hole (SMBH) in the Galactic center, or dark matter annihilation. SNIa remain an intriguing, but serious candidate, with a potential Galactic yield of 2 10^{43} e^+ s^{-1} (assuming an escape fraction of 4%).

Positron energy: Radioactive decay produces positrons of energy ≤1 MeV (typical of differences between nuclear energy levels), naturally fulfilling the observational constraint on continuum γ-rays from in flight annihilation. The same applies to pair creation through γ – γ collisions in the inner accretion disk or at the base of the jets of low mass X-ray binaries (LMXRBs), microquasars and the SMBH at the Galactic center. Conversely, pair creation involving very high energy photons, as in e.g. pulsars or magnetars, produces positrons of too high energy.

The same holds for energetic p-p collisions in Galactic cosmic rays or in the baryonic jets of LMXRBs, microquasars and the Galactic SMBH. Those processes produce e^+ of energy >30 MeV, thus may be discarded as major e^+ sources in the Milky Way. Also, that same constraint limits the mass of putative decaying or annihilating DM particles to <10 MeV, while it does not constrain the mass of de-exciting DM particles.

Source morphology: None of the e^+ sources reproduces the large bulge-to-disk ratio~1 ratio inferred from SPI data. The best-established e^+ sources, β^+ decay from Al-26 and Ti-44 produced in massive stars, yield a bulge-to-disk ratio ≤ 0.2, as derived from the observed distribution of the 1.8 MeV line of Al-26 (Fig. 7). Such a distribution reflects essentially the corresponding present star formation rates in the bulge and the disk. On the other hand, an older stellar population, reflecting the time-integrated rather than the present-day star formation, is expected to have a larger bulge/disk ratio (due to the inside-out formation of the Milky Way). Binaries involving low mass stars, such as SNIa, novae and LMXRBs, are expected to have a steeper longitude profile, with a maximal bulge-to-disk ratio≤0.5 (see Prantzos et al. 2011 for a review of the expected profiles of the various candidate sources in the Galaxy).

The morphology of the observed 511 keV emission provides also some interesting constraints in the case of dark matter particles as positron sources (under the assumption of negligible e^+ propagation) (as analysed in Ascasibar et al. 2006): i) Particle candidates with velocity dependent cross section are excluded as the main source of 511 keV emission, ii) Decaying dark matter cannot be the main source of low energy positrons, because the resulting flux profile is too flat, compared to SPI data. Notice that this latter feature is a generic property of all models involving decaying particles, where the positron production (and annihilation) rate is proportional to the DM density profile: even cuspy profiles, such as the often used Navarro-Frenk-White profile, do not provide a γ-ray flux profile sufficiently peaked towards the inner Galaxy. Annihilating or de-exciting DM produces positrons at a rate proportional to the square of the DM density profile and leads to a much more peaked γ-ray profile. Light scalar annihilating particles remain a possible candidate, provided the dark matter halo is at least as cuspy as the Navarro-Frenk-White profile with γ ~ 1; however, astrophysical evidence favors flatter DM halo profiles

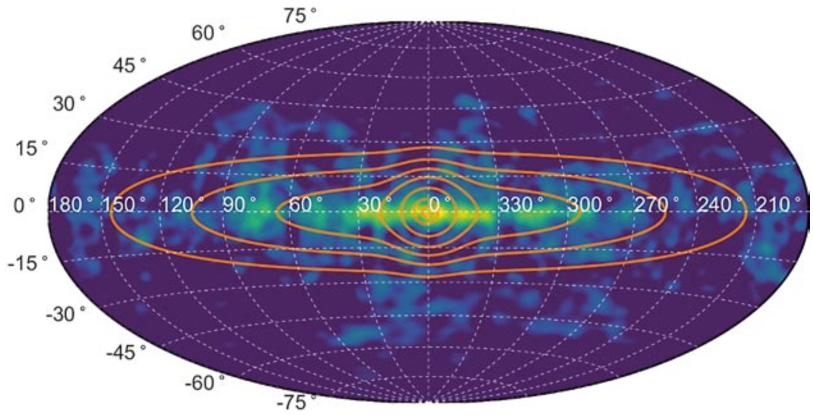

Figure 7: *Image of the Milky Way in the light of the 1.8 MeV emission (from radioactive decay of Al-26, coloured disk area) and of the 511 keV emission (from positron annihilation, over-plotted iso-contours); courtesy: R. Diehl.*

The main features of all these candidate e^+ sources are summarized in Table I. The e^+ production rates of all those sources are extremely uncertain (except those of Al-26, Ti-44 and cosmic rays) and the values listed should be considered as optimistic rather than typical ones. Only in the case of novae may the estimated production value be used to eliminate that source as important e^+ producer. Source morphology and high energy of produced positrons appear to exclude pulsars, magnetars and Galactic cosmic rays as major contributors to the observed 511 keV emission from the bulge. Source morphology alone would exclude core collapse supernova (CCSN), hypernovae and gamma-ray burst (all of them being concentrated in the Galactic disk). The high energy of positrons disfavours millisecond (ms) pulsars, as well as p-p collisions from any source (micro-quasars, LMXRB jets, the central SMBH).

A rare sub-class of SNIa, named after their 'prototype', SN1991bg, has been recently suggested as the main source of Galactic positrons (Crocker et al. 2017). That class represents ~15% of all SNIa and they are several times less luminous than the average SNIa. Theoretical — and still uncertain — models find that their explosion may produce up to a few 0.01 M⊙ of Ti-44, providing enough positrons to explain the observed 511 keV emission *and* its Galactic distribution. To obtain that, Crocker et al. (2017) assume that the Delay Time Distribution (DTD) of those objects is different than the one of standard SNIa, i.e. that it peaks several Gy after the formation of the progenitor stars (in contrast to the DTD ∝ time^{-1} of typical SNIa); one finds then that the early enhanced star formation in the bulge may produce today few SNIa but enough SNIbg to provide a large B/D ratio. Moreover, that scenario might also explain the paucity of Galactic sources of Ti-44: that radionuclide is the progenitor of stable Ca-44 and, if the source of the solar abundance of the latter is CCSN of low Ti-44 yield (as usually assumed), one should expect several SN remnants glowing in the Ti-44 γ-ray lines to be seen by ESA's INTEGRAL satellite, whereas only CasA is currently detected. The possibility of explaining at one stroke both the Galactic 511 keV emission and the paucity of 44 Ti sources makes the idea appealing. However, two key ingredients of the model, namely the Ti-44 yields and the evolution of the rate of SNIbg-type supernovae should be substantiated by further studies (including 3D models of supernova nucleosynthesis) before concluding.

If positrons annihilate near their sources, one has to conclude that (i) either poorly understood class of sources (like SNIbg-like objects) dominates e^+ production, or that (ii) positrons are produced by a combination of the sources of Table I, e.g. (a) Al-26 + Ti-44 for the disk and dark matter for the bulge, or (b) Al-44 + Ti-44 + LMXRBs (or microquasars) for the disk and the bulge plus a contribution from the central SMBH for the inner bulge, or (c) some other combination.

In order to alleviate the morphology problem, it has been suggested that positron transport might help. Prantzos (2006) suggested that if the magnetic field of the Milky Way halo has a strong poloidal component, then some positrons escaping the disk may be channelled into the bulge and annihilate there, enhancing the bulge/disk e^+ annihilation ratio. In that case, positrons from SNIa may suffice to explain quantitatively both the total observed e^+ annihilation rate (~2 10^{43} e^+ s^{-1}) and the corresponding bulge-to-disk ratio, provided that the escaping e^+ fraction from SNIa is ~3-4%. However, observations of external spirals suggest rather an X-shaped halo field in which case it would be difficult for disk positrons to find their way into the bulge. Still, the issue is of considerable interest to urge a better assessment of the poorly known global configuration of the Galactic magnetic field.

In the same framework of "outside-in" positron transport, Higdon et al (2009) suggested that positron propagation through the Galaxy may be all that is needed for understanding not only the spatial morphology of the 511 keV emission, but also its spectral properties. They assumed that radioactivity (from Al-26, Ti-44 and, mostly, from Co-56 of SNIa) is the sole e^+ source in the Galaxy and they considered (i) a fairly detailed description of the various phases of the ISM and (ii) a particular phenomenological model of collisionless scattering of MeV positrons by turbulent fluctuations of the interstellar medium (ISM), allowing to transport positrons from the inner 3 kpc into the bulge region.

The aforementioned ideas were put in test through detailed numerical simulations of positron transport, either with Monte Carlo methods (Alexis et al, 2014) or with cosmic ray propagation codes (Martin et al, 2012). In both cases, it was found that, although positrons may travel up to a few kpc from their birth place, the bulk of them is annihilated rather close to their birth places, making it difficult to reproduce the observed high B/D ratio; re-acceleration of positrons, not considered in those studies, might help in that respect.

Finally, the idea of an "inside-out" propagation of positrons was explored,

Source	Process	$E(e^+)^a$ (MeV)	e^+ rate^b $\dot{N}_{e^+}$ (10^{43} s^{-1})	Bulge/^{c} Disk^c B/D	Comments
Massive stars: ^{26}Al	β^+	$\sim$1	0.4	<0.2	$\dot{N}, B/D$: Observationally inferred
Supernovae: ^{44}Ti	β^+	$\sim$1	0.3	<0.2	$\dot{N}$: Robust estimate
SNIa: ^{56}Ni	β^+	$\sim$1	2	<0.5	Assuming $f_{e^+,esc}$=0.04
SN91bg-like: ^{44}Ti	β^+	1	4	$\sim$0.5	Assuming 0.03 $M_\odot$ of ^{44}Ti per SN
Novae	β^+	$\sim$1	*0.02*	<0.5	Insufficent e^+ production
Hypern./GRB: ^{56}Ni	β^+	$\sim$1	?	<0.2	Improbable in inner MW
Cosmic rays	p-p	~30	0.1	<0.2	Too high e^+ energy
LMXRBs	$\gamma-\gamma$	$\sim$1	*2*	<0.5	Assuming L_{e^+} ~0.01 $L_{obs,X}$
Microquasars	$\gamma-\gamma$	$\sim$ 1	*1*	<0.5	e^+ load of jets uncertain
Pulsars	$\gamma-\gamma$	>30	*0.5*	<0.2	Too high e^+ energy
ms pulsars	$\gamma-\gamma$	>30	*0.15*	<0.5	Too high e^+ energy
Magnetars	$\gamma-\gamma$	>30	*0.16*	<0.2	Too high e^+ energy
Central black hole	p-p	High	?		
	$\gamma-\gamma$	1	?		Requires e^+ diffusion to $\sim$1 kpc
Dark matter	Annih.	1 (?)	?		Light scalar particle, cuspy DM profile
	Deexcit.	1	?		Only cuspy DM profiles allowed
	Decay	1	?		Ruled out for all DM profiles
Observational constraints		<7	2	1.4	

a: typical values are given. *b*: e^+ rates: in roman: observationally deduced or reasonable estimates; in italic: speculative (and rather closer to upper limits). *c*: sources are simply classified as belonging to either young (B/D <0.2) or old(<0.5) stellar populations.

Table 1: *Properties of candidate positron sources in the Milky Way (adapted from Prantzos et al. 2011)*

a: typical values are given. b: e+ rates: in roman: observationally deduced or reasonable estimates; in italic: speculative (and rather closer to upper limits). c: sources are simply classified as belonging to either young (B/D<0.2) or old (B/D<0.5 stellar populations.

in order to investigate the possibility of positrons produced by the activity of a central Galactic source (the super-massive black hole of SgA in the Galactic center) and diffusing throughout the bulge. The spectral signature of the 511 keV emission, suggesting that positrons annihilate mostly in the warm ISM, provides a powerful constraint in that case. The Monte Carlo study of Jean et al (2009b) investigated collisional transport in the ISM of the bulge and found the diffusion length of positrons to exceed typical size scales of the warm ISM, where they are thought to annihilate. On the other hand, Panther et al (2018) investigated the transport of positrons coupled to the turbulent, magnetized plasma outflowing from the inner Galaxy (as evidenced from infra-red and γ-ray observations). They found that although positrons may indeed be advected to scales of ~2 kpc and fill the bulge, they would annihilate mostly in a hot, ionized plasma, while observations point to a warm ISM. That study concerns a steady plasma and positron outflow, while Alexis et al. (2014b) argued that a burst of activity in the galactic center 1-10 My ago could make positrons annihilate in a warm environment, in agreement with observations.

In summary, more than 40 years after its discovery, the origin of positrons annihilating in the Galaxy remains unknown. Progress in the field will require advances in several directions:

(i) Observations of 511 keV emission: what is the true spatial distribution of the emission? how far the spheroid and disk extend? are there yet undetected regions of low surface brightness? is the disk emission asymmetric indeed? how do the 1.8 MeV and 511 keV disk emissions compare to each other? A much deeper exposure of the Galaxy and a better understanding of the backgrounds will be required to tackle those issues. Even if INTEGRAL's mission is extended to 2028, it seems improbable that it will be able to provide the answers; and no other mission in this energy range is scheduled at present.

(ii) Physics of e^+ sources: what is the e^+ escaping fraction in SNIa? what is the SNIa rate in the inner (star forming) and in the outer (inactive) bulge? what are the e^+ yields, activity timescales, and spatial distribution in the inner bulge of LMXRBs or microquasars? how can the past level of activity of the central massive black hole be reliably monitored?

(iii) Positron propagation: what is the large scale configuration of the Galactic magnetic field? what are the properties of interstellar plasma turbulence and how they affect the positron transport? what are the dominant propagation modes of positrons and what the role of re-acceleration might be?

The many facets of the Galactic 511 keV emission make this problem one of the most intriguing problems in high energy astrophysics today and for the years to come.

References

Alexis, A.; Jean, P.; Martin, P.; Ferrière, K. 2014, A&A 564, 491

Anderson, C. D., 1932, Science 76, 238.

Ascasibar, Y., P. Jean, C. Boehm, and J. Knoedlseder, 2006, Mon. Not. Roy. Astron. Soc. 368, 169

Blackett, P. M. S., and G. P. S. Occhialini, 1933, Royal Society of London Proceedings Series A 139, 699

Bussard, R.W., R. Ramaty, and R. J. Drachman, 1979, ApJ 228, 928.

Crocker, R. M.; Ruiter, A. J.; Seitenzahl, I. R.; Panther, F. H.; Sim, S.; Baumgardt, H.; Möller, A.; Nataf, D. M.; Ferrario, L.; Eldridge, J. J.; 2017, Nature Astronomy, Volume 1, id. 0135

de Shong, J. A., R. H. Hildebrand, and P. Meyer, 1964, Physical Review Letters 12, 3.

Deutsch, M., 1951, Physical Review 82, 455

Dirac, P.A. M., 1931, Royal Society of London Proceedings Series A133, 60

Joliot, F., and I. Curie, 1934, Nature 133, 201

Ginzburg, V. L., 1956, Nuovo Cimento, Suppl.X 3, 38.

Guessoum, N., R. Ramaty, and R. E. Lingenfelter, 1991, ApJ 378, 170.

Guessoum, N., P. Jean, and N. Prantzos, 2006, A&A 457, 753

Higdon, J. C., R. E. Lingenfelter, and R. E. Rothschild, 2009, ApJ 698, 350.

Jean, P., J. Knödlseder, W. Gillard, N. Guessoum, K. Ferrière, A. Marcowith, V. Lonjou, and J. P. Roques, 2006, A&A 445, 579.

Jean, P.; Gillard, W.; Marcowith, A.; Ferrière, K. 2009, A&A 508, 1099.

Johnson, W. N., F. R. Harnden, and R. C. Haymes, 1972, ApJ 172, L1+.

Kinzer, R. L., P. A. Milne, and J. D. Kurfess, 2001, ApJ 559, 282+.

Klemperer, O., and J. Chadwick, 1934, Mathematical Proceedings of the Cambridge Philosophical Society 30, 347

Knodlseder, J., P. Jean, V. Lonjou, G. Weidenspointner, N. Guessoum, W. Gillard, G. Skinner, P. von Ballmoos, G. Vedrenne, J.-P. Roques, S. Schanne, B. Teegarden, et al., 2005, A&A 441, 513

Leventhal, M., C. J. MacCallum, and P. D. Stang, 1978, ApJ 225, 11+

Martin, P.; Strong, A.W.; Jean, P.; Alexis, A.; Diehl, R. 2012, A&A 519, 100

Mohorovicic, S., 1934, Astronomische Nachrichten 253, 93.

Ore, A., and J. L. Powell, 1949, Physical Review 75, 1696.

Panther, F.H.; Crocker, R. M.; Birnboim, Y.; Seitenzahl, I. R.; Ruiter, A. J. 2018, MNRAS 474, L17.

Pollack, J. B., and G. G. Fazio, 1963, Physical Review 131, 2684

Prantzos, N., 2006, A&A 449, 869.

Prantzos, N., 2008, New Astronomy Review 52, 457.

Prantzos N., 2017, Nature Astronomy 1, id. 0149.

Prantzos, N.; Boehm, C.; Bykov, A. M.; Diehl, R.; Ferrière, K.; Guessoum, N.; Jean, P.; Knoedlseder, J.; Marcowith, A.; Moskalenko, I. V.; Strong, A. and Weidenspointner G., 2011, Reviews of Modern Physics 83, 1001.

Purcell, W. R., L.-X. Cheng, and D. D. Dixon, 1997, ApJ 491, 725+.

Siegert, T.; Diehl, R.; Khachatryan, G.; Krause, M. G. H.; Guglielmetti, F.; Greiner, J.; Strong, A. W.; Zhang, X., 2016, A&A 595, A25

Sizun, P., M. Cassé, and S. Schanne, 2006, Phys. Rev. D 74 (6), 06351

Weidenspointner, G., G. Skinner, P. Jean, J. Knödlseder, P. von Ballmoos, G. Bignami, R. Diehl, A.W. Strong, B. Cordier, S. Schanne, and C. Winkler, 2008a, Nature 451, 159

Heliospheric Imaging from Solar Orbiter and Parker Solar Probe

by Angelos Vourlidas

SO/SoloHI & PSP/WIPSR Project Scientist, Johns Hopkins University Applied Physics Laboratory, Laurel, MD, USA.
Also at IAASARS, Observatory of Athens, Penteli, Greece

Abstract:

Pioneered by Coriolis/SMEI and established by the STEREO/SECCHI HIs, imaging of the inner heliosphere has breathed fresh air in Heliophysics. The regular availability of synoptic, spatially resolved images of transients and quiescent solar wind structures as they propagate from the corona to 1 AU and beyond is driving major advances in our understanding of the inner heliosphere and is bringing the space physics and solar communities together. Heliospheric imaging is about to enter a new and exciting phase thanks to two unprecedented space missions, Parker Solar Probe (PSP) and Solar Orbiter (SO), to be launched in 2018 and 2020, respectively. These missions are designed to enter the solar atmosphere (PSP) and give us our first direct view of the solar poles (SO). They will attack the solar wind problem head-on with comprehensive suites of remote sensing and in-situ instruments. Here, I provide an overview of the missions and discuss the capabilities, science opportunities and peculiarities of heliospheric imaging from the PSP and SO heliospheric imagers.

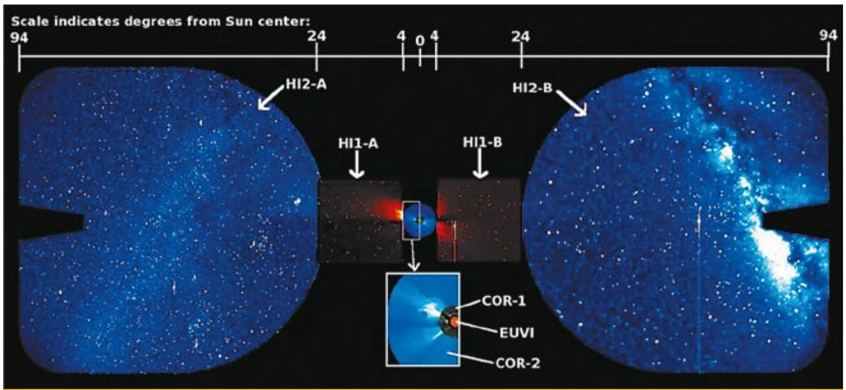

Figure 1: *The combined field of view of the SECCHI instrument suite from both STEREO spacecraft. COR1-2 are the SECCHI coronagraphs and EUVI is the EUV disk imager (only the EUVI from the STEREO-A spacecraft is shown). The planets Mercury and Venus are in the HI1-B and HI2-B images, respectively, marked by the vertical stripes (the HIs lack shutters). The Milky Way dominates the HI2-B view.*

Introduction

The inner heliosphere – the volume of space that encloses the inner planets – is where the influence of the Sun holds supreme. Here, the quiescent plasma outflow from the solar corona becomes solar wind and the more explosive transients, called Coronal Mass Ejections (CMEs), develop and release energy in interactions with the solar wind, other CMEs, and the planets. The CME-induced disturbances on the planetary magnetospheres and ionospheres are known as Space Weather (SpW) and are of particular importance to Earth. The effects from a disturbed magnetosphere can wreak havoc on the satellite systems we rely on for telecommunications, security, and disaster monitoring, to name a few. SpW can even affect the ground transmission of electrical power during extreme events. Therefore, it is critical to understand how CMEs and the ambient solar wind evolve in the inner heliosphere in order to improve our SpW predictions. At the same time, the investigation of the interactions between CMEs and the ambient solar wind is important for many fundamental research areas, including kinetic processes in plasmas, magnetic reconnection, the evolution of shocks and the transport of energetic particles accelerated in them. Fundamental research and SpW applications meet in the inner heliosphere.

The inner heliosphere, however, is a vast region of space, studied primarily by in-situ probes, such as Helios, or planetary missions on route to their targets. While these missions have returned a wealth of data, those data are on small spatial scales generally lacking the large-scale context. Rudimentary imaging from the Helios photometers indicated that interplanetary CMEs could be observed (Jackson 1985). The principle was proven with the deployment of the Solar Mass Ejection Imager (SMEI; Eyles et al. 2003) – a collection of photometers, relying on the rotation of the host spacecraft to map the sky from 20° to 180° elongation from the Sun. Because of the low spatial resolution and sensitivity, SMEI detected CMEs only as narrow arcs in the sky making associations with events seen closer to the Sun ambiguous. The large angular gap, from 8° to 20°, between SMEI and the Large Angle Spectrometric and Coronagraph (LASCO; Brueckner et al. 1995) C3 coronagraph exasperated the problem (Morrill et al. 2009). Eventually, SMEI observed several hundred CMEs, until its shutdown in 2011, with an effective spatial resolution of a couple of degrees demonstrating the feasibility of heliospheric imaging (Howard et al. 2013).

True heliospheric imaging became possible with the launch of the Solar Terrestrial Relations Observatory (STEREO; Kaiser et al. 2008) mission and the deployment of the Heliospheric Imager (HI) package (Eyles et al. 2009) within the Sun-Earth Connection Coronal and Heliospheric Investigation (SECCHI; Howard et al. 2008) payload (Figure 1). Quasi-identical SECCHI instrument suites operate on both STEREO spacecraft which are separating at opposite sites from Earth at a rate of 22.5° per year. The package comprising two conventional telescopes (HI-1 and HI-2) with fields of view of 20° and 70° and spatial resolutions of ~51" and 3 arc min, respectively, has revolutionized the field. For the first time, we are able to compare in-situ measurements through a transient with images of the transient taken at the same time over the same location, and from two viewpoints to boot!

Although an extensive review is beyond the scope of this paper (see also Vourlidas 2011), the following small collection of results demonstrates the large range of science enabled by heliospheric imaging. The HIs have imaged and tracked not only CMEs (Rouillard et al. 2009a) but also streamer interaction regions (SIRs) impinging on Earth (Sheeley et al. 2008), small flux ropes entrained in the SIRs (Rouillard et a. 2009b) and even small-scale structures embedded within the slow solar wind (Sheeley & Rouillard 2010). The imaging capability has particularly benefited space weather studies. The error in the time of arrival of CMEs at Earth has improved from about 24 hours prior to STEREO to 5-7 hours now (e.g. Millward et al. 2012; Colaninno et al. 2013). It is recognized that CMEs may rotate, deflect, distort (Isavnin, Vourlidas & Kilpua 2014; Nieves-Chinchilla et al. 2012), and interact with each other (e.g. Shen et al. 2013), on their way to Earth.

It should probably come as no surprise that heliospheric imaging has raised many new questions. Despite the comprehensive imaging coverage, reconstructions of the CME structure from in-situ and imaging disagree (Wood et al. 2017). The arrival time can be off by several hours even when the CME is seen overtaking Earth in the HI images. The kinematic profile of medium speed (< 900 km/s) interplanetary CMEs (ICMEs) is difficult to measure precisely as they decelerate very gradually (Colaninno et al. 2013). Projection effects may lead to apparent rotations or propagation direction changes (Nieves-Chinchilla et al. 2012). Many of the discrepancies arise because neither the precise trajectory of the in-situ spacecraft through the transient nor the 3D geometry of the CME are known with sufficient detail. Many events are difficult to track beyond the middle of the HI-1 field of view (FOV), above about 50-60 solar radii (Rs), for example. The extremely low brightness of ICMEs (10^{-13-14} of the solar disk brightness) requires very long exposure times and the use of running difference schemes to increase contrast both of which obscure the fine structure within the ICMEs.

Fortunately, the field of heliospheric imaging is about to enter a new stage with the launch of two extraordinary Heliophysics missions. The Parker Solar Probe (PSP), scheduled for launch in July 2018, will reach within 9.86 Rs from Sun center, the smallest ever perihelion of a manmade probe. Solar Orbiter (SO), scheduled for launch no earlier than February 2020, will climb to 34° out of the ecliptic, providing our first ever view of the solar poles and a completely new perspective on the inner heliosphere. Both missions carry heliospheric imagers that open exciting science opportunities for Heliophysics and Space Weather research.

I discuss these science opportunities below. In the next section, I summarize the PSP science objectives and concept of operations for context, describe the objectives and operation of the PSP heliospheric imager, and discuss the implications for heliospheric imaging. I present the same information for SO in the following section. I present some issues that arise from these unusual orbits and conclude in Section 4.

Heliospheric Imaging from the Parker Solar Probe Mission

PSP is the most ambitious Heliophysics mission to date. The spacecraft, via a series of Venus Gravity Assists (VGA), will achieve a perihelion of just 9.86 Rs form Sun center. This will be humanity's first foray into a stellar atmosphere to measure the basic properties of the solar wind (temperature, density, velocity, energetic particle populations) at the region of its formation.

Science Objectives

The PSP science is described in detail in Fox et al. (2016). The objectives of the mission are to determine the structure and dynamics of the Sun's coronal magnetic field, understand how the solar corona and wind are heated and accelerated, and determine what mechanisms accelerate and transport energetic particles.

Payload

To achieve such close perihelia, the spacecraft has to expend large amounts of kinetic energy which in turn restricts the mass available for payloads. In addition, the heat flux at the front of the spacecraft will be 475x higher than at Earth, at the closest approach. The large temperatures (~1400 °C) require the use of a uniform heat shield without any openings so no solar pointing telescopes are possible. For these reasons, the PSP payload is restricted to four instruments:

- **The Fields Experiment (FIELDS; Bale et al. 2016)**: This investigation will make direct measurements of electric and magnetic fields and waves, Poynting flux, absolute plasma density and electron temperature, spacecraft floating potential and density fluctuations, and radio emissions.
- **Solar Wind Electrons Alphas and Protons (SWEAP) Investigation (Casper et al. 2016)**: This investigation will count the most abundant particles in the solar wind – electrons, protons and helium ions – and measure their properties such as velocity, density, and temperature.
- **Integrated Science Investigation of the Sun (IS⊙IS; McComas et al. 2016)**: This investigation makes observations of energetic electrons, protons and heavy ions that are accelerated to high energies (10s of keV to 100 MeV) in the Sun's atmosphere and inner heliosphere and correlates them with solar wind and coronal structures.
- **Wide-field Imager for Solar PRobe (WISPR; Vourlidas et al. 2016)**: These telescopes will image the solar corona and inner heliosphere. The experiment will also provide images of the solar wind, shocks and other structures as they approach and pass the spacecraft. The investigation complements the other PSP instruments by imaging the plasma the other instruments sample.

In addition to the payloads, PSP includes a science investigation as a 'payload':

- **Heliospheric origins with Solar Probe Plus (HeliOSPP)**: The HE-

LIOSPP PI (M. Velli) serves as the Observatory Scientist for the PSP Project and carries out an inter-disciplinary science investigation that focuses on the goals and objectives of the PSP mission. He serves on the PSP SWG and provides independent (from the instrument PIs) input to the PSP Project Scientist.

Concept of Operations

PSP is an encounter mission – nominal science operations occur only when the spacecraft is within 0.25 AU from Sun (Figure 2). This translates to a temporal window of 10-11 days around the perihelion of a given orbit. The remainder of the orbit is devoted to data downlinks, spacecraft operations, and instrument calibrations. The orbit period decreases as the spacecraft gets closer to the Sun. Science planning for the upcoming two orbits starts 6 months in advance within the PSP Science Working Team (SWT). The SWT defines the science targets, allocates data volume reserves to particular instruments and coordinates with other space or ground assets. Instruments teams upload their final plans sometime before the start of the science window.

The WISPR Imager

Vourlidas et al. (2016) provide a comprehensive description of the WISPR instrument and science investigation. In a nutshell, WISPR comprises two visible broadband telescopes ('inner' & 'outer') with a combined FOV of 95° radial x 58° transverse (Figure 3) and is the smallest HI built to date. The instrument concept is very similar to the SECCHI/HI (Howard et al. 2008). A series of linear baffles intercept the diffracted light from the edge of the PSP shield while a cover, with two openings for the telescope apertures, captures stray light from the FIELDS antennas which are located just behind the shield. The instrument is located on the PSP ram side. The most important instrument parameters are summarized in Table 1 and a representation of the WISPR FOVs onto a SECCHI image composite is shown in Figure 4. The instrument uses the PSP heat shield as its first occulter. With the addition of safety margins for spacecraft offpoints, the inner FOV cutoff is set at 13.5° elongation from Sun center. The inner telescope observes from 13.5° to 53.5° elongation and the outer from 50° to 108°. The wide FOV is driven by two requirements: (1) capture a substantial part of the corona as the spacecraft approaches the Sun and (2) image the plasma structures to be intercepted by the spacecraft, which are located at around 90° elongation.

Being the sole imager on PSP, WISPR has the primary task to link the PSP in-situ measurements with the large-scale structure of the corona to address the PSP science objectives above. But WISPR will also provide unique science, such as two-dimensional electron density power spectra, and observations of interplanetary dust, and sungrazing comets, that will

Instrument Parameter	WISPR	SoloHI
Field of View	Inner: 40° x 40° Outer: 58° x 58°	40° x 40°
Spatial Resolution	Inner: 2.34 arc min Outer: 3.38 arc min	2.4 arc min
Cadence range	1 sec → 15 min	10 sec → 15 min
Bandpass	Inner: 490 – 740 nm Outer: 475 – 725 nm	500-700 nm
Detector	2048x1920 APS, 10 μm pixel	2x2 mosaic of 2948x1920 APS, 10 μm pixel
Average Power	7 W	13.1 W
Mass	9.8 kg	14.8 kg
Data Volume Allocation	23 Gbits/orbit	53.2 Gbits/orbit

Table 1: *Top-level instrument parameters for the WISPR and SoloHI imagers.*

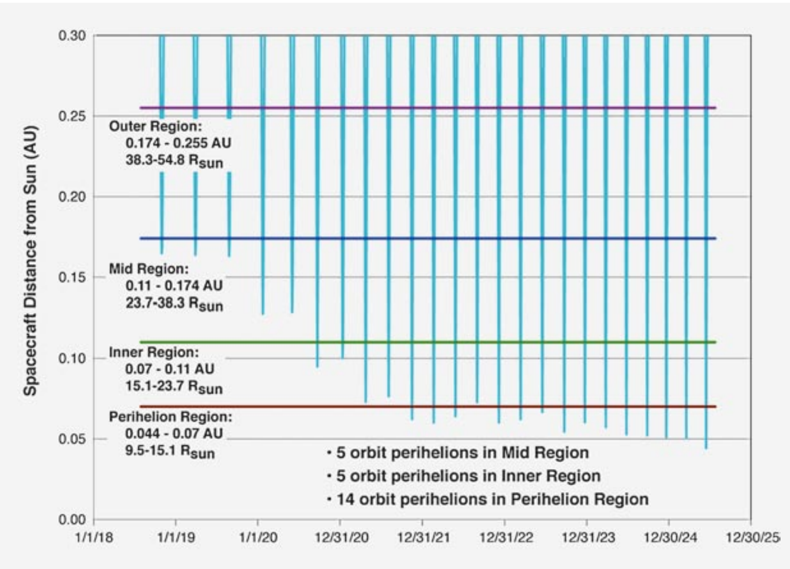

Figure 2: *The PSP heliocentric distance for the duration of the nominal mission. The regions mark locations where the WISPR observing program and science focus changes.*

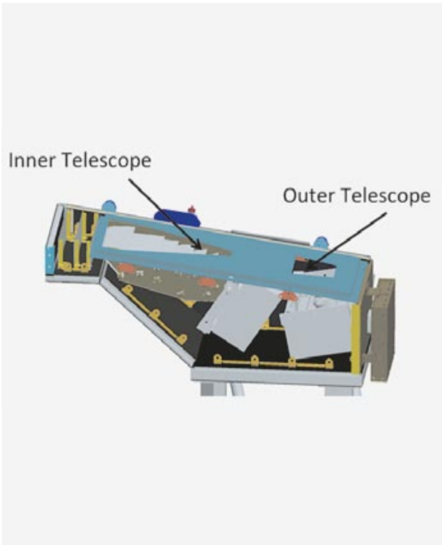

Figure 3: *Cutaway of the WISPR telescope module showing the linear baffles, the aperture hood, and the two telescope assemblies.*

greatly enhance the mission science. The unique science is enabled by the highly elliptical PSP orbit with its rapidly varying heliocentric distance. It is quite distinct from the almost circular ~1AU orbits of the STEREO spacecraft. Imaging from WISPR will be very different than the heliospheric imaging from STEREO we are used to.

First, the rapidly varying distance results in variable FOV and spatial resolution. The FOV shrinks and the resolution increases as PSP approaches perihelion and vice versa as it moves away from the Sun. Table 2 compares some representative spatial resolution values to other coronagraphs and HIs to give an idea of the effect. In other words, WISPR *'zooms'* in and out of the corona during a typical science orbit (i.e. starting at 0.25 AU), providing the large-scale context near the start/end of the science window and imaging small scales around perihelion.

Second, the spacecraft angular velocity increases as the perihelia reduce. At the nearest perihelion of 9.86 Rs, the spacecraft will be moving at about 6 arcsec/sec. Consequently, WISPR will sweep over a considerable heliolongitude range during perihelion; it will rotate faster than the Sun sweeping through the corona. In other words, WISPR will perform a *'CAT scan'* of the corona around perihelion. The resulting images could be used to reconstruct the 3D structure of the corona. Algorithms for this so-called Solar Rotational Tomography (SRT) were developed for coronagraphs observations (Vásquez et al. 2008) but the angular coverage from 1 AU is too slow to account properly for the coronal evolution. WISPR offers a unique opportunity to use the SRT methodology to obtain the 3D electron density distribution of the inner corona.

Third, a welcomed benefit of the orbit profile is solar corotation. There is a period in each orbit, starting with orbit 1, where PSP is rotating at the same angular speed as the Sun *while it is moving radially inwards*. Measuring the corotation duration as the time it takes PSP to cross the size of a supergranule (~30,000 km), the corotation period is about one day for the earlier orbits, reducing to about 0.6 days towards the end of the mission. During corotation, the corona will effectively 'freeze' in the WISPR FOV, allowing separation of radially moving features from rotational and Thompson scattering effects (discussed later). This will also be an extremely interesting period for the in-situ instruments because they will be scanning the radial structure of the solar wind along the *same* set of field lines.

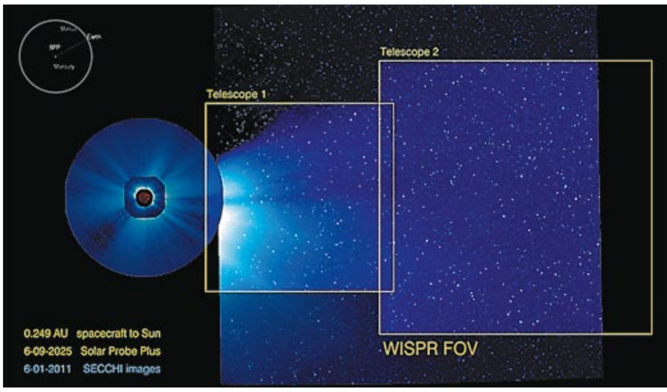

Figure 4: *The field of view of WISPR's two telescopes superimposed on a composite of the SECCHI telescopes (all but HI-2) and scaled to the viewing geometry on June 9, 2025 at 0.25 AU heliocentric distance.*

Telescope	Heliocentric Distance (AU)	FOV (R_s AU$_{eq}$)	Spatial Resolution (arcsec AU$_{eq}$)
WISPR	0.25 0.046	9.5 – 83 2.5 – 20	35 – 50 6.5 – 9.3
SoloHI	0.28	5.1 – 47	25
LASCO/C2	1	2.2 – 6	24
SECCHI/COR2	1	2.5 – 15	30
SECCHI/HI1	1	15 – 90	108
SECCHI/HI2	1	74 – 337	250
SMEI	1	74 →337	1440

Table 2: *Comparison of the FOV and resolution of several operating coronagraphs and imagers to the SoloHI and WISPR. Adapted from Vourlidas et al. (2016).*

Fourth, as PSP enters the corona from even the first perihelion (at 35 Rs), WISPR is going to give us a view of the corona we never had before. The telescopes will image the corona from the *'inside'*. WISPR will approach and eventually cross though streamers or coronal holes, revealing their substructures, if they exist, at an ever-finer scale. Note that the spatial resolutions quoted in Table 2 are for objects at infinity. There is no restriction to the size of the spatial scale, when the feature is in the near field, as long as the feature has sufficient signal-to-noise ratio to be detected by the instrument. Hence, it is conceivable that WISPR may detect current sheets (actually the plasma sheets surrounding them) if they are dense enough (say a few thousand e/cm^3 within a sub-1000 km sheet).

Fifth, WISPR will provide the first images of the corona virtually free from the contributions of the interplanetary dust. The emission from the dust, called the F-corona or zodiacal light (at large elongations from the Sun) dominates the visible emission beyond about 5 Rs and has to be removed from the coronagraph or HI images to recover the emission from the coronal electrons (Stenborg & Howard 2017). But since WISPR operates only within 0.25 AU from the Sun, the majority of the dust will lie outside the instrument's FOV resulting in much reduced F-corona contributions and much brighter coronal emission that lead to new findings about the structure and evolution of the corona. Additionally, the reduced F-corona foreground emission may allow WISPR to establish whether a dust free zone exists near the Sun (< 4Rs) as postulated by Russell (1929). If it exists, then the rate at which the F-corona brightness diminishes in the vicinity of the dust-free zone may enable to model the composition of the dust (Mann et al. 2004).

Additional unique science opportunities, regarding comets and other objects, are discussed in Vourlidas et al. (2016). The WISPR images will also be used for more familiar analyses, such as CME and shock 3D reconstructions with supporting observations from SECCHI, LASCO, and SoloHI, tracing blobs and jets, etc.

Heliospheric Imaging from the Solar Orbiter Mission

Solar Orbiter mission is a European Space Agency (ESA) with NASA contributions (launcher, instrumentation). The spacecraft will make a series of VGAs to gradually tilt its orbital plane to a final inclination of 34° relative to the ecliptic. Similar to PSP, it is an inner heliospheric mission with nearest perihelion of 0.28 AU.

Science Objectives

The SO mission is described in detail in Müller et al. (2013). The SO objectives are to determine the origins of the solar wind plasma and magnetic field, understand how transients drive heliospheric variability and produce energetic particles and investigate how the solar dynamo works and drives connections between the Sun and the heliosphere. The objectives are somewhat similar to the PSP objectives but SO is more focused on the solar magnetic field and its evolution as it will provide our first view of the solar poles and most accurate measurements of polar magnetic fields to date.

Payload

Because SO perihelia are farther from the Sun than PSP's, the SO heat shield can accommodate aperture openings, so there are several sun-pointed telescopes on board. As the mass constraints are also more relaxed than PSP, the spacecraft is able to carry 4 in-situ and 6 remote sensing instruments (Table 3).

Acronym	Instrument Name	PI	Description
In-situ Instruments			
EPD	Energetic Particle Detector	J. Rodríguez - Pacheco	Composition, timing and distribution functions of energetic particles
MAG	Magnetometer	T. Horbury	High-precision measurements of the heliospheric magnetic field
RPW	Radio & Plasma Waves	M. Maksimovic	Electromagnetic and electrostatic waves, magnetic and electric fields at high time resolution
SWA	Solar Wind Analyzer	C. Owen	Sampling protons, electrons and heavy ions in the solar wind
Remote Sensing Instruments			
EUI	Extreme Ultraviolet Imager	P. Rochus	High-resolution and full-disk EUV imaging of the on-disk corona
METIS	Coronagraph	E. Antonucci	Visible and UV Imaging of the off-disk corona
PHI	Polarimetric & Helioseismic Imager	S. Solanki	High-resolution vector magnetic field, line-of-sight velocity in photosphere, visible imaging
SoloHI	Heliospheric Imager	R. Howard	Wide-field visible imaging of the solar off-disk corona
SPICE	Spectral Imaging of the Coronal Environment	European-led facility instrument	EUV spectroscopy of the solar disk and near-Sun corona
STIX	Spectrometer/Telescope for Imaging X-rays	S. Krucker	Imaging spectroscopy of solar X-ray emission

Table 3: *The Solar Orbiter Science Payload.*

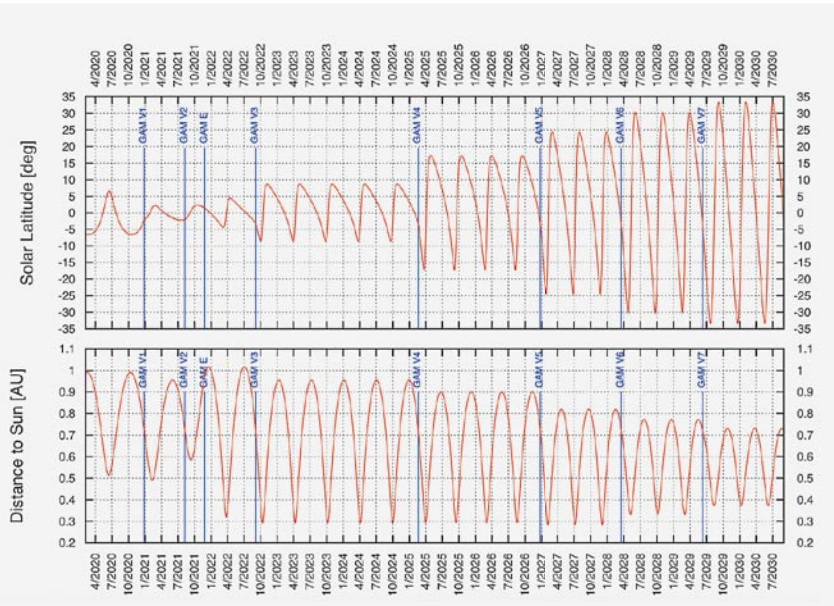

Figure 5: *The Solar Orbiter orbit profile for the February 2020 launch option.*

Concept of Operations

Because of the use of a smaller launcher than PSP, SO adopts a cruise phase with an Earth gravity assist to reach Venus (Figure 5). The cruise phase is 1.8 years, for the earliest possible launch date on February 2020 (we use this launch option in the remainder) during which the remote sensing instruments are powered off, except for occasional checkouts every few months or so. The in-situ instruments, however, are powered on after the spacecraft and instrument checkouts and take measurements throughout the cruise phase.

At the end of the cruise phase, the remote sensing instruments come online and the nominal science phase begins around March 2022. The concept of operations for the remote sensing payload is similar to PSP. The payloads operate only when the spacecraft is within 0.5 AU but only for 30 days, split into 10-day observing windows. The windows may or may not be contiguous. At the moment, they are located around each perihelion and the latitudinal extremes of each orbit (which may fall outside 0.5 AU for the latter orbits). The

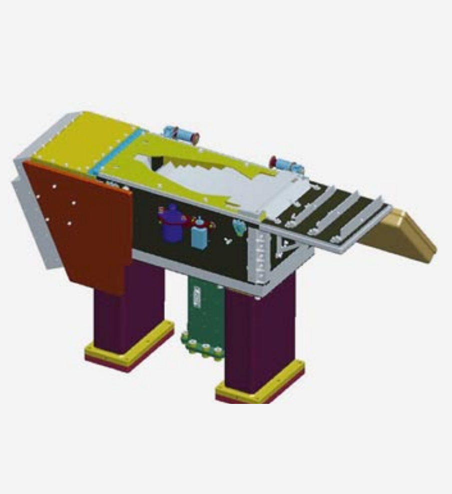

Figure 6: *The SOloHI Instrument.*

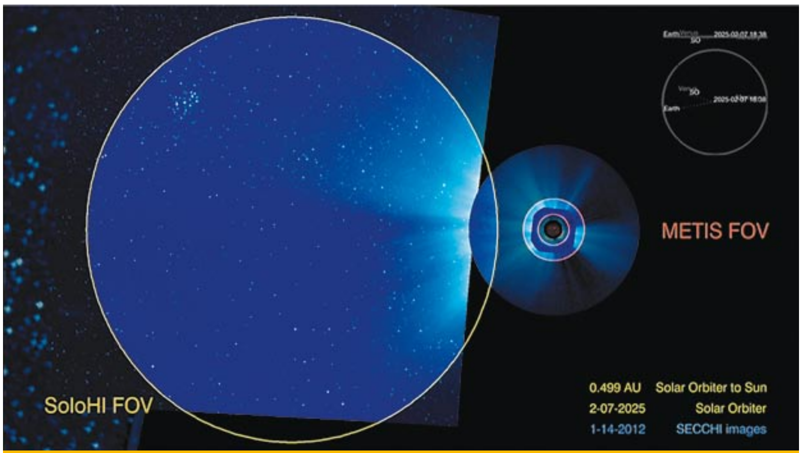

Figure 7: *The field of view of SoloHI superimposed on a SECCHI telescope composite and scaled to the viewing geometry on February 7, 2025 at a heliocentric distance of 0.5 AU. The METIS FOV is also drawn showing a 2.5° gap between the two telescopes.*

science planning cycle begins in the Solar Orbiter Science Working Group (SWG) six months before each orbit to define the Long-Term Plan (LTP). A second cycle, the Medium-Term Plan (MTP) refines those plans with detailed instruments activities ending about 4 weeks before the first science window. Finally, a Short-Term Plan (STP), takes into account any changes in solar activity, target selections and other small corrections and is uploaded 2-3 days before execution.

The SoloHI Imager

The Solar Orbiter Heliospheric Imager (SOloHI) investigation is described in Howard et al. (2013). It is a single visible broadband telescope with a 40° × 40° FOV (Figure 6) extending from 5.5° to 45° solar elongation. It uses a set of linear baffles to capture the diffracted light from the heat shield and an aperture cover to prevent stray light from other spacecraft structures, such as the RPW antenna. The SoloHI instrument parameters are shown in Table 1 and a representation of the instrument FOV on a SECCHI composite is shown in Figure 7. The telescope is located on the anti-ram side of the spacecraft. Therefore, SoloHI images the corona *after* the SO passage and hence its science is more focused on the connectivity with the other imagers (EUI, STIX, SPICE) rather than with the in-situ instrumentation.

SoloHI primary science tasks are: (1) provide the link between the SO disk imagers and the in-situ payloads, (2) provide the link between the SO and PSP missions, and (3) follow the evolution of CME, shocks, and SIRs. Similar to WISPR, SoloHI will also make observations of sungrazing comets, interplanetary dust, and acquire electron density power spectra, from a unique viewpoint away from the ecliptic. In that sense, the WISPR and SoloHI investigations are highly complementary as they view the corona from completely novel perspectives. The unusual SO orbit creates a similar set of capabilities to WISPR; namely, variable FOV and resolution, reduced F-corona contribution, and longitudinal coverage for tomography. But the effects are reduced compared to WISPR because of the larger perihelion. However, SoloHI has the unique ability to image the corona and inner heliosphere from *'above'* which leads to two considerations: Thompson scattering effects and rotational effects.

Because the scattering depends only on the angle between the scattering volume and the observer and the heliocentric distance of that volume, CMEs and other structures will not appear intrinsically different from *'above'*. Since the scattering remains relatively flat for angular distances up to about 30°-40° from the sky plane, we expect projection effects on the CME only late in the mission when the orbit is close to the maximum inclination. Nevertheless, SoloHI will provide constraints for CME reconstructions since it will be observing the events from much closer than STEREO. We will likely learn new things about the internal structure and extent of CMEs if/when events are captured simultaneously by WISPR, SoloHI and STEREO.

The most novel aspect of the large inclination is the viewing of the heliosphere from close to the rotational axis of the Sun. The solar rotation is responsible for the familiar Parker spiral effect on the magnetic field and the 'garden hose' structure of SIRs and Corotating Interaction Regions (CIRs). Restricted within the ecliptic, all previous coronagraphs or HIs has been unable to image that structure directly. For that reason, it is unclear at which height the coronal magnetic field stops rotating rigidly with the rest of the corona, how CIRs form, how and why they tend to entrain flux ropes. Even the interaction between CMEs and the ambient wind will be much clearer with heliospheric imaging from large inclinations.

Heliospheric Imaging Issues

Finally, we discuss some of the common issues facing the data reduction from WISPR and SoloHI. Those are: background subtraction, kinematics measurements, and synoptic coverage. Because the F-corona and stray light are significant contributors to the detected signal in coronagraphs and HIs, the background needs to be removed before performing any science analysis. Several techniques have been developed over the years and forming the median (or minimum) of the emission over an extended time series (months to years) is the most common one. It is used by default in LASCO and SECCHI coronagraph images. This approach will not work for WISPR and SoloHI because the background scene, spatial resolution and stellar fields are constantly changing. Our current approach is to form a model for each image separately. A preliminary effort shows great promise when applied to SECCHI/HI images (Stenborg & Howard 2017) but the proper validation needs to wait until the first WISPR images.

Measuring the height versus time of structures (i.e. CME fronts, small-scale blobs and jets) to derive their kinematics is a well-established analysis method in the field (e.g. Lugaz et al. 2009; Davies et al. 2013; Möstl et al. 2014). Different techniques rely on various assumptions about the motion and properties of the source (i.e. radial propagation, self-similar expansion, small extent along the line-of-sight) but they all make a fundamental assumption – the observer motion relative to the source is insignificant. *This is not the case* for SoloHI or WISPR. Particularly for WISPR, the PSP spacecraft will reach tangential speeds of about 190 km/s at the 9.86 Rs perihelion. These speeds are comparable, and quite possibly higher, that the solar wind speed at those heights. In addition, the PSP-feature distance can change appreciably during the measurement. This will affect the shape of the height-time curve, and hence of the speed derived from a fit as shown in the Figure 8 examples. Slow features will be overtaken by the spacecraft resulting in rapidly 'decelerating' curves (100 km/s case). On other hand, faster features will exhibit rapid acceleration. The trajectories for all features will be different between PSP (and SO to a lesser degree) and 1 AU spacecraft, such as STEREO. Joint analyses, therefore, will likely provide crucial information about the speed and location of the blobs in space, as long as the same features can be reliably identified among the various imagers.

Finally, it should be apparent from the concept of operations of both missions, that WISPR and SoloHI cannot provide the synoptic 24x7 coverage of the solar activity we have been accustomed to in the SOHO and STEREO eras. The instruments will observe only for small periods in each orbit (10 and 30 days, respectively). Both, however, will allocate part of their telemetry budget to a synoptic program (i.e. regular cadence sequences of full FOV images) during their observing windows. The lack of synoptic coverage reduces the utility of both missions for SpW operations but does not diminish their potential for SpW research. The opportunity to resolve CME substructures, including the shock, and generally measure the state of the inner heliosphere from varying viewpoints from both in and outside the ecliptic is bound to advance our understanding of the transient solar wind structures by leaps and bounds.

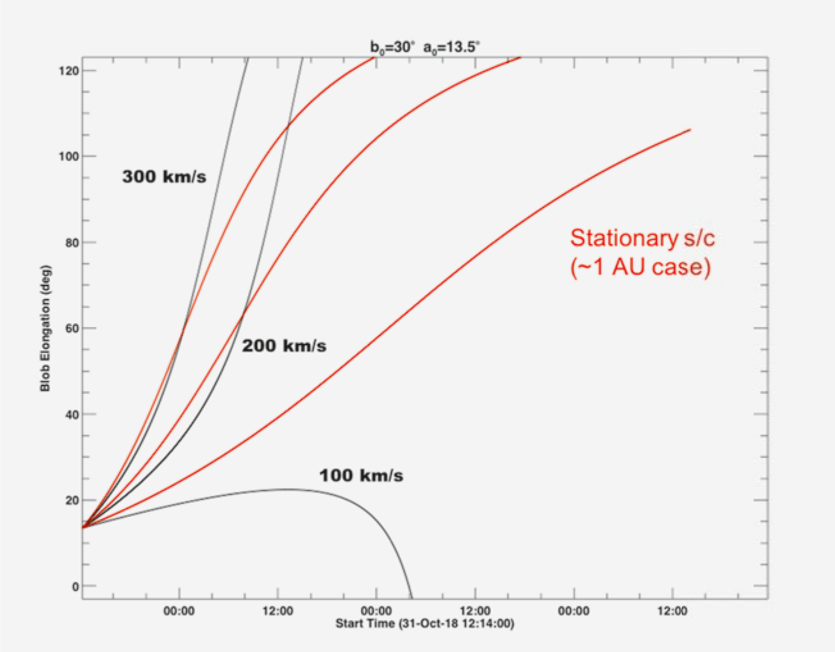

Figure 8: *Simulated trajectories of 3 blobs propagating at constant speeds (marked on the plot) through the WISPR FOV starting at the inner edge (13.5° elongation) at 30° from the spacecraft during the 9.86 Rs perihelion. The red curves show the same trajectories for a spacecraft at 1 AU.*

Conclusions

In this introductory article, I attempted a sweeping overview of the two major upcoming Heliophysics missions of PSP and SO with an emphasis on their heliospheric imaging aspects. Both missions employ innovative and technically challenging orbits which extend our measuring capabilities to uncharted areas of the inner heliosphere. Consequently, PSP and SO are different that previous solar imaging missions in several ways that I try to summarize in the following list:

- **Concept of Operations**: PSP and SO are encounter missions, akin to planetary missions. They are not synoptic missions like STEREO. Each orbit will likely have specific targets and go after specific science objectives.
- **Data**: Due to orbital constraints, observations from each orbit will be downlinked weeks or months after their acquisition. There is no real-time capability and hence no direct SpW operational application.
- **Coordination**: Solar wind physics is the primary science target and design justification for PSP and is high priority for SO (with polar magnetic field measurements being its primary science). Therefore, the science focus is on linkage between the in-situ measurements and the solar sources. The effective coordination and collaboration between the in-situ and remote sensing teams drives mission success to a much larger degree than past Heliophysics missions.
- **Viewpoint**: Remote sensing science is challenged and simultaneously empowered by the continuously varying heliocentric distance and changing viewpoint.
- **Science Targets**: The orbits and science objectives of SO and PSP put emphasis on quiescent structures, kinetic scales, and the background structure of the corona. Activity-related analyses, such as 3D CME structure, shocks or SEPs observations although extremely valuable, may be very few and serendipitous.

The heliospheric imaging from WISPR and SoloHI can benefit substantially from strong synergies with other visible light telescopes, such as the coronagraphs on STEREO, SOHO (if still operational). Off-limb spectroscopy, currently unavailable, could provide critical measurements (speeds, densities, composition) at heights close to but inaccessible by PSP. Ground-based facilities, particularly InterPlanetary Scintillation (IPS) arrays (not discussed here) can contribute and augment the science return from either mission. Potential contributions to PSP from several ground-based facilities are discussed in a white paper (https://sppgway.jhuapl.edu/sites/default/files/Pubs/SPP-GBN-WhitePaper-v5.0.pdf)

In closing, I hope that this short article conveys the great science opportunities and discovery potential from the heliospheric imaging afforded by the Parker Solar Probe and Solar Orbiter missions. We are about to embark on the greatest exploration journey of our generation – enter into the atmosphere of the Sun and view the solar poles for the first time. We will need all the help we can get to make sense of the observations. Let's go explore!

Acknowledgements

A.V.'s effort in the WISPR and SoloHI projects is supported by NASA WISPR contract and by NRL grant N00173-16-1-G029, respectively. I thank Dr. Y. Zouganelis for providing Figure 5. The paper is based on a presentation at the "Into the Red Dragon's Lair: Four-in-One Workshop Tackling Outstanding Problems in Heliophysics and Space Weather" meeting held on Dec 3-8, 2017 at Cardiff, UK. A.V. thanks the organizers for the invitation to discuss the subject of heliospheric imaging.

References

Bale, S. D. *et al.* The FIELDS Instrument Suite for Solar Probe Plus. *Space Sci Rev* **204,** 49–82 (2016).

Brueckner, G. E. *et al.* The Large Angle Spectroscopic Coronagraph (LASCO). *Solar Physics* **162,** 357–402 (1995)

Colaninno, R. C., Vourlidas, A. & Wu, C. C. Quantitative Comparison of Methods for Predicting the Arrival of Coronal Mass Ejections at Earth Based on Multiview Imaging. *Journal of Geophysical Research: Space Physics* **118,** 6866–6879 (2013).

Davies, J. A. *et al.* Establishing a Stereoscopic Technique for Determining the Kinematic Properties of Solar Wind Transients based on a Generalized Self-similarly Expanding Circular Geometry. *The Astrophysical Journal* **777,** 167 (2013).

Eyles, C. J. *et al.* The Solar Mass Ejection Imager (SMEI). *Solar Physics* **217,** 319–347 (2003).

Eyles, C. J. *et al.* The Heliospheric Imagers Onboard the STEREO Mission. *Sol Phys* **254,** 387–445 (2009).

Fox, N. J. *et al.* The Solar Probe Plus Mission: Humanity's First Visit to Our Star. *Space Sci Rev* **204,** 7–48 (2016).

Howard, R. A. *et al.* Sun earth connection coronal and heliospheric investigation (SECCHI). *Space Science Reviews* **136,** 67–115 (2008).

Howard, R. A. *et al.* The solar and heliospheric imager (SoloHI) instrument for the solar orbiter mission. in *SPIE* **8862,** 88620H-88620H–13 (SPIE, 2013).

Howard, T. A. *et al.* The Solar Mass Ejection Imager and Its Heliospheric Imaging Legacy. *Space Sci Rev* **180,** 1–38 (2013).

Isavnin, A., Vourlidas, A. & Kilpua, E. K. J. Three-Dimensional Evolution of Flux-Rope CMEs and Its Relation to the Local Orientation of the Heliospheric Current Sheet. *Sol Phys* **289,** 2141–2156 (2014).

Jackson, B.V. Imaging of coronal mass ejections by the HELIOS spacecraft. *Solar Physics* **100,** 563–574 (1985).

Kaiser, M. L. *et al.* The STEREO Mission: An Introduction. *Space Science Reviews* **136,** 5–16 (2008).

Kasper, J. C. *et al.* Solar Wind Electrons Alphas and Protons (SWEAP) Investigation: Design of the Solar Wind and Coronal Plasma Instrument Suite for Solar Probe Plus. *Space Sci Rev* **204,** 131–186 (2016).

Lugaz, N., Vourlidas, A. & Roussev, I. I. Deriving the radial distances of wide coronal mass ejections from elongation measurements in the heliosphere – Application to CME-CME interaction. *Annales Geophysicae* **27,** 3479–3488 (2009).

Mann, I. *et al.* Dust Near the Sun. *Space Science Reviews* **110,** 269–305 (2004).

McComas, D. J. *et al.* Integrated Science Investigation of the Sun (ISIS): Design of the Energetic Particle Investigation. *Space Sci Rev* **204,** 187–256 (2016).

Millward, G., Biesecker, D., Pizzo, V. & de Koning, C. A. An operational software tool for the analysis of coronagraph images: Determining CME parameters for input into the WSA-Enlil heliospheric model. *Space Weather* **11,** 57–68 (2013).

Morrill, J., Howard, R., Vourlidas, A., Webb, D. & Kunkel, V. The Impact of Geometry on Observations of CME Brightness and Propagation. *Solar Physics* **259,** 179–197 (2009).

Möstl, C. *et al.* Connecting Speeds, Directions and Arrival Times of 22 Coronal Mass Ejections from the Sun to 1 AU. *The Astrophysical Journal* **787,** 119 (2014).

Müller, D., Marsden, R. G., Cyr, O. C. S. & Gilbert, H. R. Solar Orbiter. *Sol Phys* **285,** 25–70 (2013).

Nieves-Chinchilla, T. *et al.* Remote and in situ observations of an unusual Earth-directed coronal mass ejection from multiple viewpoints. *Journal of Geophysical Research (Space Physics)* **117,** 06106 (2012).

Rouillard, A. P. *et al.* A solar storm observed from the Sun to Venus using the STEREO, Venus Express, and MESSENGER spacecraft. *Journal of Geophysical Research (Space Physics)* **114,** 07106 (2009a).

Rouillard, A. P. *et al.* A Multispacecraft Analysis of a Small-Scale Transient Entrained by Solar Wind Streams. *Solar Physics* **256,** 307–326 (2009b).

H.N. Russell, On meteoric matter near the stars. Astrophys. J. **69,** 49 (1929)

Sheeley, N. R. *et al.* Heliospheric Images of the Solar Wind at Earth. *Astrophysical Journal* **675,** 853–862 (2008).

Sheeley, N. R. & Rouillard, A. P. Tracking Streamer Blobs into the Heliosphere. *The Astrophysical Journal* **715,** 300–309 (2010).

Shen, C. *et al.* Super-elastic collision of large-scale magnetized plasmoids in the heliosphere. *Nature Physics* **8,** 923 (2012).

Stenborg, G. & Howard, R. A. A Heuristic Approach to Remove the Background Intensity on White-light Solar Images. I. STEREO/HI-1 Heliospheric Images. *The Astrophysical Journal* **839,** 68 (2017).

Vásquez, A. M. *et al.* Validation of Two MHD Models of the Solar Corona with Rotational Tomography. *The Astrophysical Journal* **682,** 1328–1337 (2008).

Vourlidas, A. Recent Advances in Heliophysics from Space-Based Observations. *Hipparchos* **2,** 37–44 (2011).

Vourlidas, A. *et al.* The Wide-Field Imager for Solar Probe Plus (WISPR). *Space Sci Rev* **204,** 83–130 (2016).

Wood, B. E. *et al.* A STEREO Survey of Magnetic Cloud Coronal Mass Ejections Observed at Earth in 2008-2012. *The Astrophysical Journal Supplement Series* **229,** 29 (2017).

The Hellenic Radiotelescope THERMOpYlae

by Nectaria A.B. Gizani[1] and **Giorgos P. Veldes**[2], on behalf of the Scientific Team.

1. School of Science and Technology, Hellenic Open University, Patra, Greece. Currently in her sabbatical leave at the Department of Astronomy at UC Berkeley,
2. Department of Electronics Engineering, TEI of Sterea Ellada

ngizani@berkeley.edu, gveldes@teiste.gr

1. Introduction

High costs accompanying the built of a new radio telescope drove the need to pursue other means of both acquiring a radiotelescope in Greece and mastering the know how in radio antenna engineering, also contributing with innovative new technologies. The advent of the scientific adventure of converting a 30m telecommunication antenna to a radio telescope will materialize within a decade in Greece.

The project is the result of the scientific collaboration between the School of Science and Technology (SST) of the Hellenic Open University (HOU) and the Telecommunication Systems & Applications Research Laboratory (TSARL) of the Department of Electronics Engineering of the Technological Educational Institute (TEI) of Sterea Ellada. A Memorandum of Understanding was signed between the owner of the antenna, the Hellenic Telecommunication Company (OTE), and SST-HOU /TSARL-TEI. with which OTE granted to the Institutes the use of the equipment to convert it to a professional radiotelescope of international standards. OTE supports the project fully with electricity costs and some pre- and after- maintenance.

The conversion we are planning to undertake is not attempted for the first time. Currently such antennas are being transformed in the world, as there is a dual gain obtained from such an action: Less expensive, but efficient radio astronomical equipment and Knowledge. Woodburn, *et al.*, 2015 [doi:10.1017/pasa.2015.13] and references therein, has succeeded in a similar transformation we propose, enjoying at present a fully scientific instrument. In fact, Woodburn and collaborators have worked on an antenna very similar to ours. Current project (July 2017) is the transformed Ghana n'Kutunse telescope for the SKA (Square Kilometre Array) Africa project (https://www.ska.ac.za/media-releases/ghana-and-south-africa-celebrate-first-success-of-african-network-of-telescopes/).

Figure 1:
Photo of the C-band Satellite Telecommunications Antenna (photo credit OTE)

2. Infrastructure and Kick off plan

The dish (see Fig. 1) is located in Thermopile Telecommunication Station at the south-eastern point of Europe in the region of Skarfeia, Lokrida (see Fig. 2). The instrument has an alt-azimuth, wheel-and-track, Cassegrain beam-waveguide antenna, an electric-servo dual train for anti-backlash drive system, transmission and reception frequency in the *C*-band (~6.7 GHz), primary mirror diameter ~30m and sub-reflector diameter ~2.9 m. Its azimuth working range is between –180° to +180°, about the centre of azimuth travel and its elevation range between 2° to 92°.

The project will be kicked off by using the existing C-band feed system, installing a dual polarization 6 GHz receiver with low noise amplifiers and making pointing and sensitivity amplitude and phase measurements and adjustments. A receiver bandwidth of 300MHz is adequate for professional observations. RFI environment measurements at the station will take place. The antennas seen in Fig. 2 are not currently in use, but naturally we will check shadowing and cross-talk effects.

After making an evaluation study of the moving and other parts of the dish infrastructure, we will change, accordingly, motors, cables, driving and control systems, and encoders which will allow for the adequate mechanical performance for a fully steerable professional radiotelescope. For example, the telescope should be able to quickly change targets, picking the quickest path, while slewing from one object to another.

Design and installation of cables allowing total azimuth movement (± 270°), is a requirement in a professional instrument. Limit switching will be implemented to protect the antenna from unwanted movement (eg. driving past safe azimuth and elevation movement limits). Oiling mechanical maintenance, further focused cleaning, replacing rusty and malfunctioning parts, anti-rust surfacing, painting, of the dish itself and its supporting structure, etc will undoubtedly take place.

For the backend we will need to purchase new radio astronomy digitization electronics, such as digital base band converter, a VLBI recorder, a snapboard, etc. There is a plethora of astronomy Institutes that are currently involved in building digitization electronics and we can make use of: for example new design snapboards are being produced at UC Berkeley (Project Casper) and at CSIRO; Broad band receivers are being built within RadioNet and used at Onsala in the new VGOS antennas and so on.

Further, optical fibres will be tested as needed since we need to transmit the astronomical signal to correlators/processing centres. Software will be implemented to enable source tracking in celestial coordinates, as the telecommunications antenna was manufactured to track geostationary satellites.

3. Work Plan and Innovation

Our scope after acquiring the know - how of the C-band functionality is to operate the antenna at L-band with the vision to go higher (≥10 GHz).

Figure 2: *The Thermopile Telecommunication Station (38°49'20.74"N 22°41'9.51"E) owned by the Hellenic Telecommunication Company OTE (from google-earth).*

Our project's innovation will be the design and construction of a receiver which will operate in L-band in two different frequency ranges (eg. 1200-1450 MHz and 1600-1700 MHz). In general, a dual-band (DB) component is a component accomplishing the same function at two different arbitrary frequencies without the need to design two different mono-band circuits. In our receiver this will be achieved by using the theory and techniques of the CRLH TL metamaterials. The CRLH TL allows arbitrary dual-band operation as a benefit of its four degrees of freedom. This feature does not exist in conventional transmission lines and thus we cannot design DB components. As a result, our radiotelescope will operate as dual band radiotelescope with the same receiver.

The future Hellenic radioastronomy facility includes incorporating other large diameter antennas as seen for example in Figure 2.

4. Scientific Outcome and National Impact

We are aiming to a 30m antenna with state of the art functionality: The radiotelescope will be a fully professional instrument capable of observing, *both as a stand-alone single dish and also linked in the Very Long Baseline Interferometry (eg. EVN, VLBI), thus* increasing the sensitivity of the interferometer(s). *Both spectral line and continuum modes will be enabled.* In the interferometry mode the antenna can be used to perform space geodetic studies and participate to international geodetic surveys (International VLBI Service for Geodesy & Astrometry), using a wide range of frequencies from 1.3GHz, for example, all the way to 10GHz (L-, S-, C-, X-, K-bands).

The dish will also participate in SETI searches with appropriate backend in collaboration with the Breakthrough Listen Research Laboratory, of the Department of Astronomy, of the UC Berkeley.

The national impact, expected from our project, includes inspirational drive for new scientists as a result of popularization and educational activities in the scientific field of Radioastronomy, the opening of new fields of applications which could contribute to the development of the Hellenic Industry, etc.

A short video of the antenna at its location can be found in OTE's youtube channel in the following link:

https://www.youtube.com/watch?v=adYggTk7g-E

Astronomical conferences and workshops in Greece during 2017

As we do every year, in the following pages you can find brief presentations of the conferences, which took place in Greece during 2017 and for which the organizers sent us a summary of their main results. Of course during 2017 took place also our 13th Hellenic Astronomical Conference, for which one can find details in the web pages of our society. The presentations in the current issue of "Hipparchos", refer to the following meetings:

- "The Labyrinth of the Unexpected: The unforeseen treasures in impossible regions of phase space", 29 May - 3 June 2017, Kerastari, Arcadia
- "The Greek Scientific Participation in Solar Orbiter / ESA mission: Perspectives & Outlook", June 6, 2107, Institute for Astronomy, Astrophysics, Space Applications and Remote Sensing (IAASARS) of the National Observatory of Athens (NOA)
- "Polarised Emission from Astrophysical Jets", June 12-16, 2017, Ierapetra
- "Kappa Distributions and Statistical Mechanics in Space and Astrophysical Plasmas", 10-14 July 2017, Corfu, Kerkyra

1 The Labyrinth of the Unexpected: unforeseen treasures in impossible regions of phase space

29 May - 3 June 2017, Kerastari, Arcadia

About every 5 years in the village of Kerastari in the ancient region of Arcadia in Greece experts in radio astronomy from all around the world meet to discuss their latest scientific discoveries and astronomical techniques. These international workshops are organized by Dr Tasso Tzioumis who was born in Kerastari but lives in Australia and works in CSIRO.

Details of previous workshops in 2002, 2007, 2012 can be found at <https://www.atnf.csiro.au/people/Tasso.Tzioumis/>.

This workshop on **"The Labyrinth of the Unexpected: unforeseen treasures in impossible regions of phase space"** has a very specific rationale:

To explore how radio astronomy has enabled flexible processing environments that are opening new windows on the Universe (discovery of Fast Radio Bursts (FRB) is the prime example) and may open others e.g. for the Search of Extra Terrestrial Intelligence (SETI). How have unexpected discoveries unfolded in a technical sense and in the new/traditional fora for scientific debate? Has anything benefited the process or held it back?

As we enter the era of the SKA, are we prepared for the technical challenges and, more importantly, do we have people prepared for serendipity? Or are we preparing a generation of SKA users to blindly extract data from catalogues to produce plots? Do these questions matter?

The workshop attracted 60 registered participants from all over the world. The main themes for the program were FRBs, SETI and the Transient Discovery Space, and how to maximize serendipity in the SKA era. Also covered were Radio Frequency Interference (RFI) and its impact on discoveries; Propagation effects in the ISM/IGM; New telescopes, instrumentation and techniques; and multi-wavelength, multi-messenger exploration.

Details of the program and the new scientific results presented at the workshop are available at

http://www.atnf.csiro.au/research/conferences/2017/Labyrinth/

including copies of all the presentations and many photos. An excellent introduction is the Summary of the Labyrinth Workshop.

A highlight of the meeting was also the exploration of the natural beauty and glorious history of the region, especially the traditional Greek hospitality.

Finally, we must acknowledge the generous sponsorship and support by the locals in Kerastari, the Municipality of Tripoli, the regional government (Periphereia Peloponnisou), and our international sponsors from CSIRO, CAASTRO and RadioNet.

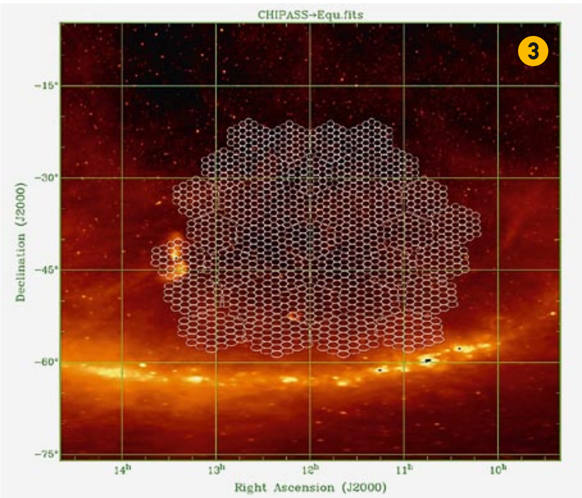

Figure 1. Workshop Venue. Old school at Kerastari. **Figure 2.** Conference participants photo. **Figure 3.** Search for Fast Radio Bursts (FRB) with ASKAP Phased Array Feeds (PAF) in "fly's-eye" mode, using the 36 ASKAP antennas x 36 beams to search a large part of the sky simultaneously. (Credit: Keith Bannister, CSIRO)

2

Workshop on the "Greek Scientific Participation in Solar Orbiter / ESA mission: Perspectives & Outlook"

June 6, 2017

The Institute for Astronomy, Astrophysics, Space Applications and Remote Sensing (IAASARS) of the National Observatory of Athens (NOA) organized on June 6, 2107 a full-day workshop on the "Greek Scientific Participation in Solar Orbiter / ESA mission: Perspectives & Outlook". The workshop was by invitation only and it was attended by 23 participants from National Research Centers and Universities.

The scope of the Workshop was to:

(a) inform the Greek Scientific Community on Solar Orbiter's instruments and scientific goals

(b) discuss the scientific synergy between Solar Orbiter and NASA's Solar Probe Plus mission

(c) explore the perspectives of the Greek scientific participation.

Invited presentations was given by Dr. Yannis Zouganelis, Deputy Project Scientist of Solar Orbiter (ESA/ESAC) and Dr. Angelos Vourlidas, Solar Physics Section Supervisor at JHU/APL, followed by a discussion session where the participants presented targeted, relevant to the Solar Orbiter scientific objectives, proposals.

The organization of the Workshop was supported by the IAASARS/NOA, the RCAAM of the Academy of Athens and the Hel.A.S. More information about the workshop and access to the presentations can be found at:

http://proteus.space.noa.gr/~forspef/solar_orbiter

On behalf of the Scientific Organizing Committee

Dr. Anastasios Anastasiadis
Research Director at IAASARS/NOA

3

Conference: Polarised Emission from Astrophysical Jets

June 12-16, 2017, Ierapetra, Greece

The conference aimed at a comprehensive coverage of the **theoretical** and **observational** aspects related to the **linearly** and **circularly** polarized emission observed from astrophysical jets; both **extragalactic** and **galactic**. It was hosted by the Foundation of Cultural and Social Care of the Metropole of Ierapetra and Sitia in Ierapetra on the southern coast of eastern Crete in the prefecture of Lasithi. It was organized by the Max-Planck-Institut für Radioastronomie with the support of Metropole of Ierapetra and Sitia, the Municipality of Ierapetra and RadioNet.

The Scientific Organizing Committee included **Emmanouil Angelakis** (*Max-Planck-Institut für Radioastronomie*, Germany), **Markus Boettcher** (*Centre for Space Research, North-West University, South Africa*), **Rob Fender** *(Department of Physics, University of Oxford. UK)*, **Jose Luis Gomez** *(Instituto de Astrofísica de Andalucía, Spain)*, **Talvikki Hovatta** *(Tuorla Observatory, University of Turku, Finland)* and **J. Anton Zensus** *(Max-Planck-Institut für Radioastronomie, Germany)*.

The conference was attended by more than **90 scientists** from **25 countries**. The program included **82 oral presentations** with **20** of them given by **invited speakers** reviewing an impressive canvas of subjects and **10 posters**. Links to the presentations and the posters can be found at the program page. Most of the contributions are published as refereed papers in special issue of the MDPI journal Galaxies. As it can be seen there and in the conference summary talk by Lukasz Stawarz (**Jagiellonian University, Krakow, Poland)**, practically all the relevant subjects were discussed.

Remarkably rich was also the social program which was especially designed to target the young generation of the public. It included:

1. An **astrophotography contest** in the categories of **Deep sky, Solar system** and **Landscape astrophotography.** The winning pictures were voted by the conference participants and were rewarded observing time at the 1-m telescope of the South African Astronomical Observatory and the 80-cm IAC-80 telescope of the Observatorio del Teide in Tenerife and a start tracker "Vixen Polarie Star Tracker", sponsored by "*Πλανητάριο Θεσσαλονίκης*".
2. A **public talk on the subject "Our universe step by step"** by E. Angelakis following the closing ceremony reviewing the essential astrophysical phenomena and systems using solely material from the astrophotography contest.
3. **A Star-gazing night** with guide M. Perakis in collaboration with the Cretan Friends of Astronomy (SFAK.org).
4. **Public talk on the subject "The Minoans in Time and Space"** by Dr A. MacGillivray (British School of Athens) reviewing of current thinking on the origins and interconnections of Europe's first great maritime civilization and their appreciation of the night sky for both navigation, and time keeping.
5. **Guided tour** to Gournia Minoan site by Prof. Y. Papadatos (University of Athens) and Institute for Aegean Prehistory Study Center for East Crete by its director Thomas M. Brogan.

Conference url:
https://www3.mpifr-bonn.mpg.de/old_mpifr/jetpol/jetpol/Home.html

Papers: http://www.mdpi.com/journal/galaxies/special_issues/astrophysical_jets

4

Kappa Distributions and Statistical Mechanics in Space and Astrophysical Plasmas

10-14 July 2017, Corfu, Kerkyra

The workshop on "Kappa Distributions and Statistical Mechanics in Space and Astrophysical Plasmas" is a triannual meeting held in conjunction with Sigma-Phi Conference. In 2017 the workshop was organized between 10-14 July, at the Corfu Holiday Place Hotel, Corfu, Kerkyra. (Primary Convener: G. Livadiotis, Southwest Research Institute, USA; Co-Conveners: P. Yoon, Univ. of Maryland, USA; K. Dialynas, Academy of Athens, Greece.) There were 58 abstracts submitted by distinguished scientists from world class universities (e.g., Princeton University, University of California-Berkeley, University of London, Max-Planck Institute, etc.) and over 23 countries; the abstracts were distributed as plenary, invited, contributed talks or posters.

The meeting was opened by Dr. Danny Summers, introducing the book of kappa distributions, theory and applications in plasmas, published by Elsevier few months earlier [Livadiotis, G., 2017, Kappa distributions: Theory and applications in plasmas, Elsevier, Netherlands, UK, USA; https://www.elsevier.com/books/kappa-distributions/livadiotis/978-0-12-804638-8]. The presentations were separated in several topics: Methods, Solar Atmosphere, Corona, Heliosphere, Space Weather, Magnetospherics, Plasma Waves, Turbulence, Theory of Statistical Mechanics, Theory of Kappa Distributions. Prof. X. Moussas closed the meeting with a remarkable "feature talk", entitled "The oldest computer, the Antikythera Mechanism, and the laws of physics". (Invited speakers: Chapman S.; Consolini G.; Cui X.; Dzifcakova E.; Fleishman G.; Gontikakis G.; Kourakis I.; Kucharek H.; Mace R.; Martinović M.; McComas D.; Ogasawara K.; Pavlos G.; Pierrard V.; Salem C.; Sarlis N.; Summers D.; Vocks C.; Vörös, Z.; Wang L.; Watkins N.)

The goal of the meeting was to report on the progress of the following three broad subject areas: (a) *Theory of Kappa Distributions & Statistical Mechanics Framework*. (b) *Effects on Plasma Processes, Dynamics, and Complexity*. (c) *Data Analyses, Simulations, & Applications in Space Plasmas*.

Numerous new important results were presented. Among others, we mention the following: 1) General theory of kappa distributions and applications in plasmas. 2) Temperature misestimation when Maxwell distributions are used for kappa distributed plasmas. 3) Effects of kappa distributions on plasma processes. 4) Non-extensive approach to magnetic reconnection. 5) Inhomogeneity and dynamical complexity in space plasmas. 6) Long range

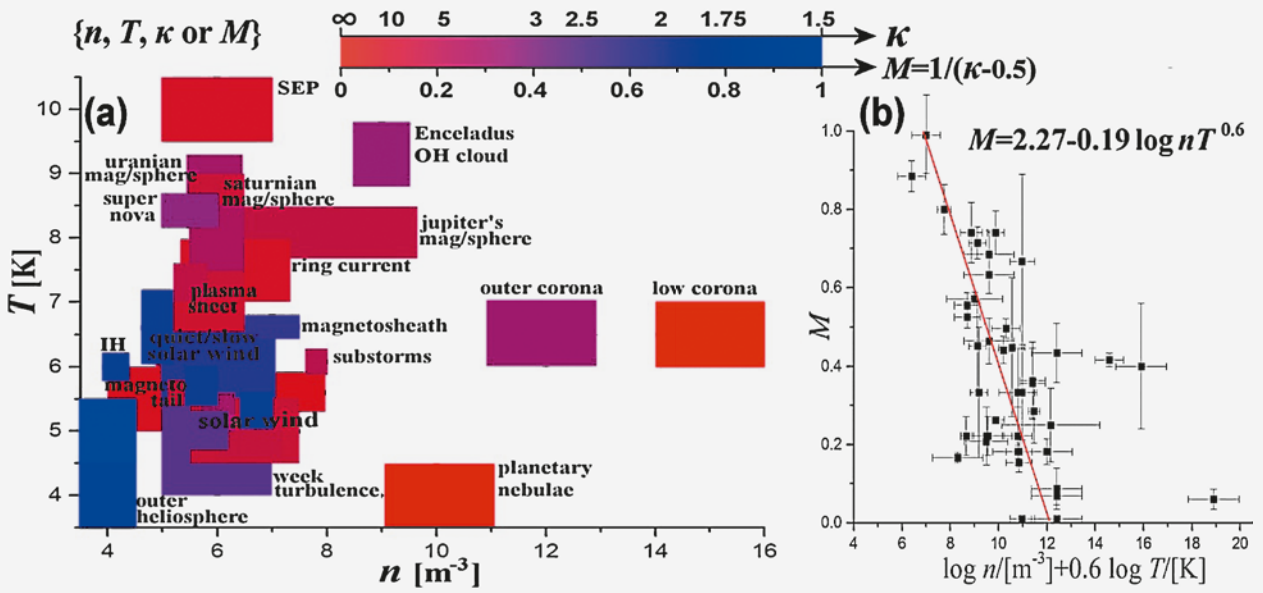

Figure 1. (a) Color-map of kappa indices for various space plasmas with different values of density n and temperature T. The kappa index κ or the measure $M=1/(\kappa-1/2)$ spans the whole interval from $\kappa \to \infty$ or $M=0$ (thermal equilibrium) to $\kappa \to 1.5$ or $M=1$ (Anti-equilibrium, i.e., the furthest state from thermal equilibrium). (b) The measure M is negatively correlated (or, the kappa index is positively correlated) with the temperature and density [modified version of a result presented in Livadiotis, G., 2015, Statistical Background and Properties of Kappa Distributions in Space Plasmas, JGR, 120, 1607.]

dependence, fractional renewal models, and Bayesian inference. 7) Effects of kappa distributions on electromagnetic ion-cyclotron waves. 8) Effects of kappa distributions on waveparticle interactions and particle dynamics. 9) Kinetic theory of Lorentzian distributed twisted waves. 10) Effects of kappa distributions on nonlinear wave-particle interactions. 11) Low frequency instabilities based on electron and ion temperature anisotropies. 12) Characteristics of electron velocity distributions in space plasmas. 13) Modelling of electrostatic solitary waves and shocks in space plasmas. 14) Kappa distribution and active regions: probing with microwave gyroresonant radiation. 15) Spectral properties of atoms/ions in kappa distributed plasmas. 16) Diagnosing kappa distributions in solar corona with polarized microwave gyro-resonance radiation. 17) Differential emission measure as a sum of gamma and kappa distributions in solar flares based on X-ray and EUV observations. 18) X-ray spectra from plasmas with high-energy electrons: kappa-distributions and bremsstrahlung. 19) Non-extensive statistical analysis of magnetic field using a multispacecraft approach. 20) In-situ observations of solar wind thermal - suprathermal electrons. 21) Determining kappa indices of space plasma distributions from limited energy range observations. 22) Effects of kappa distributions on radiation belt dynamics. 23) Properties of suprathermal electrons associated with discrete auroral arcs. 24) Kappa distributions in Saturn's magnetosphere: a model for the energetic ion moments. 25) Evolution of kappa-distributed protons downstream of the heliospheric termination shock in the presence of charge-exchange. 26) Study of suprathermal ions in the inner heliosheath plasma between the termination shock and heliopause. 27) Charging of interstellar dust grains in the nonequilibrium inner heliosheath plasma.

Further details and the abstract booklet may be found in the conference website:

http://www.sigmaphi.polito.it/attachments/article/181/_Booklet.pdf

George Livadiotis,
Southwest Research Institute

Back issues of Hipparchos

Hipparchos is the official newsletter of the Hellenic Astronomical Society. It is distributed by post to the members of the society. You can download back issues from: **http://www.helas.gr/news.php**